Title

H3K4me3 remodeling induced acquired resistance through O-GlcNAc transferase.

Authors

Ravindran Menon, Dinoop

Zuegner, Elmar

Torrano, Joachim

et al.

Publication Date

2023-11-01

DOI

10.1016/j.drup.2023.100993

Peer reviewed

HHS Public Access

Author manuscript

Drug Resist Updat. Author manuscript; available in PMC 2023 December 14.

Published in final edited form as:

Drug Resist Updat. 2023 November ; 71: 100993. doi:10.1016/j.drup.2023.100993.

H3K4me3 remodeling induced acquired resistance through O-GlcNAc transferase☆

Dinoop Ravindran Menon[a,b,c,†], **Heinz Hammerlindl**[a,d,†], **Gregory Gimenez**[e], **Sabrina Hammerlindl**[a,d], **Elmar Zuegner**[f], **Joachim Torrano**[a], **Natalie Bordag**[f], **Abdullah Al Emran**[a], **Maybelline Giam**[g], **Simon Denil**[g], **Norman Pavelka**[h], **Aik-Choon Tan**[i], **Richard A. Sturm**[a], **Nikolas K. Haass**[a], **Giulia Rancati**[g], **Meenhard Herlyn**[j], **Christoph Magnes**[f], **Michael R. Eccles**[e,k], **Mayumi Fujita**[b,l,m], **Helmut Schaider**[a,n,*]

[a]Frazer Institute, The University of Queensland, Brisbane, QLD, Australia

[b]Department of Dermatology, University of Colorado Denver, Aurora, CO, USA

[c]Department of Medical Oncology, University of Colorado Denver, Aurora, CO, USA

[d]Department of Pharmaceutical Chemistry, The University of California, San Francisco, San Francisco, CA, USA

[e]Department of Pathology, Dunedin School of Medicine, University of Otago, Dunedin, New Zealand

[f]Joanneum Research Forschungsgesellschaft m.b.H., HEALTH, Institute for Biomedicine and Health Sciences, Graz, Austria

[g]Institute of Medical Biology, Agency for Science, Technology and Research, Immunos Singapore, Singapore

[h]SIgN, the Singapore Institute for Immunology, Agency for Science, Technology and Research, Immunos Singapore, Singapore

[i]Division of Medical Oncology, Department of Medicine, University of Colorado Denver, Aurora, CO 80045, USA

[j]The Wistar Institute, Philadelphia, PA, USA

☆Dedicated to Dr Rajasekharan Somasundaram (Shyam), inspiring mind and mentor

*Correspondence to: Frazer Institute, The University of Queensland, Translational Research Institute, 37 Kent Street, Woolloongabba, QLD 4102, Australia. h.schaider@uq.edu.au (H. Schaider).

†These authors contributed equally to the study

Declaration of Competing Interest

The authors declare that they have no competing financial interests or personal relationships that influence the work reported in this paper.

CRediT authorship contribution statement

D.R.M, H.H. and **H.S**. designed the study and methodology. **D.R.M.H.H., S.H., J.T**. and **A.A.E**. acquired the data and performed the experiments. **G.G**. and **M.R.E** performed the ChIP-seq data analysis. **N.B., E.Z**. and **C.M**. performed the metabolomics measurement and data analysis. **N.K.H., R.A.S., M.F**., and **M.H**. analyzed FUCCI and *in vivo* data. **M.G., S.D., N.P**. and **G.R**. performed the mFISH karyotyping and analysis. **A.C.T**. assisted in performing PDX experiments. **D.R.M** and **H.H**. wrote the manuscript. **D.R.M**., **H.H., S.H**., **A.A.E., A.C.T., R.A.S., N.K.H, G.R., M.H., M.F., C.M., M.R.E**. and **H.S**. reviewed and revised the manuscript.

Appendix A. Supporting information

Supplementary data associated with this article can be found in the online version at doi:10.1016/j.drup.2023.100993.

[k]Maurice Wilkins Centre for Molecular Biodiscovery, Auckland, New Zealand

[l]Denver VA Medical Center, Denver, CO, USA

[m]Department of Immunology and Microbiology, University of Colorado Denver, Aurora, CO, USA

[n]Department of Dermatology, Princess Alexandra Hospital, Woolloongabba, QLD, Australia

Abstract

Aims: Drivers of the drug tolerant proliferative persister (DTPP) state have not been well investigated. Histone H3 lysine-4 trimethylation (H3K4me3), an active histone mark, might enable slow cycling drug tolerant persisters (DTP) to regain proliferative capacity. This study aimed to determine H3K4me3 transcriptionally active sites identifying a key regulator of DTPPs.

Methods: Deploying a model of adaptive cancer drug tolerance, H3K4me3 ChIP-Seq data of DTPPs guided identification of top transcription factor binding motifs. These suggested involvement of O-linked N-acetylglucosamine transferase (OGT), which was confirmed by metabolomics analysis and biochemical assays. OGT impact on DTPPs and adaptive resistance was explored *in vitro* and *in vivo*.

Results: H3K4me3 remodeling was widespread in CPG island regions and DNA binding motifs associated with O-GlcNAc marked chromatin. Accordingly, we observed an upregulation of OGT, O-GlcNAc and its binding partner TET1 in chronically treated cancer cells. Inhibition of OGT led to loss of H3K4me3 and downregulation of genes contributing to drug resistance. Genetic ablation of OGT prevented acquired drug resistance in *in vivo* models. Upstream of OGT, we identified AMPK as an actionable target. AMPK activation by acetyl salicylic acid downregulated OGT with similar effects on delaying acquired resistance.

Conclusion: Our findings uncover a fundamental mechanism of adaptive drug resistance that governs cancer cell reprogramming towards acquired drug resistance, a process that can be exploited to improve response duration and patient outcomes.

Keywords

Cellular reprogramming; Epigenetics; Metabolism; OGT; H3K4me3; TET1; Cancer persisters; Adaptive cancer drug resistance; Acquired drug resistance

1. Introduction

Acquired drug resistance is the main cause for disease relapse in metastatic cancer patients that initially respond to therapeutic intervention. Traditionally, research investigating the development of acquired drug resistance has focused on the identification of resistance mediated by genetic mutations that are often present in drug resistant tumors (Ahronian, Sennott et al. 2015, Jia et al. 2016, Manzano et al. 2016, Wang et al. 2018). Accumulating evidence now suggests the existence of an epigenetically regulated and reversible drug-tolerant state in cancer before the emergence of permanent acquired resistance (Roesch et al., 2010, Sharma et al., 2010, Hammerlindl and Schaider, 2018), which can give rise to different resistance mechanisms including *de novo* mutations (Hata et al., 2016, Ramirez et al., 2016) through a persister-like phenotype (Hong, Moriceau et al. 2018). These cancer

persisters are characterized by expression of histone demethylases (Hinohara et al., 2018) that allow for transcriptional adaption and drug tolerance (Ravindran Menon et al., 2015, Shaffer et al. 2017, Emran et al., 2018). The clinical impact of therapy-induced reversible cellular reprogramming is reflected in studies that showed delayed drug resistance following intermittent treatment schedules in a melanoma mouse model (Das et al., 2013) and the clinically meaningful re-challenge response of patients that progressed after BRAF inhibitor treatment following a short period of drug withdrawal (Tietze et al., 2018, Valpione et al., 2018). However, molecular mechanisms facilitating the shift of cancer persisters from dormant to the proliferative state remain underinvestigated.

We identified a ubiquitous cellular transition in cancer cells that drive global epigenetic reprogramming as an important factor contributing to acquired drug resistance. Specifically, the transition from the dormant drug tolerant persister (DTP) state to the proliferative drug tolerant (DTPP) state characterized by cellular clusters is achieved through upregulation of O-GlcNAc transferase (OGT) fueled by the hexosamine biosynthesis pathway. This adaption consequently leads to CpG island specific H3K4me3 remodeling. Blocking the adaptive process prolonged the treatment response to targeted- and chemotherapy, identifying OGT as a promising therapeutic target to interfere with a fundamental adaptive process that is a major obstacle for successful treatment.

2. Materials and Methods

2.1. Cell lines

Melanoma cell lines WM164, WM9, WM1366 and WM983B were obtained from The Wistar Institute. A375 were purchased from Rockland Immunochemicals Inc. Generation of FUCCI melanoma cell lines has been previously reported (Haass, Beaumont et al., 2014, Spoerri, Beaumont et al., 2017). The lung cancer cell line A549 was kindly provided by Dr. Gerald Hoefler from the Medical University of Graz, Austria. HCC827 cells were kindly provided by Dr. Derek Richard, Queensland University of Technology, Brisbane, Australia. H1975 was kindly provided by Dr. Brian Gabrielli from Mater Research Institute, The University of Queensland. All cell lines are routinely tested for mycoplasma as described previously (Uphoff and Drexler 2002, Uphoff and Drexler 2004) and were authenticated *via* STR fingerprinting. Cells were maintained in RPMI-1640 medium (Thermo Fisher Scientific), supplemented with 5% fetal bovine serum (Assaymatrix), 2% L-glutamine (Thermo Fisher Scientific) and 2% Pen/Strep (Thermo Fisher Scientific).

2.2. Inhibitors and Chemicals

Dabrafenib, trametinib, osimertinib, LY3009120 and docetaxel were purchased from Selleck Chemicals and were dissolved in DMSO for treatments. Metformin and compound C (CC) were obtained from Cayman Chemicals and dissolved in DMSO for treatments. Aspirin, Benzyl 2-acetamido-2-deoxy-α-D-galactopyranoside hydrate (BADG) and O-(2-acetamido-2deoxy-D-glucopyranosylidene)amino-N-phenylcarbamate (PUGNAc) were purchased from Sigma-Aldrich and dissolved in DMSO. OSMI-4b was kindly provided by UniQuest, The University of Queensland, Brisbane, Australia and dissolved

in DMSO. All drugs were diluted and used not exceeding a final DMSO concentration of < 0.5% (v/v).

2.3. Generation of IDTC, IDTC colonies and permanent resistant cells

Induced- drug tolerant cells (IDTCs) (Ravindran Menon et al., 2015), equivalent to drug tolerant persister (DTP) cells, and IDTC colonies, equivalent to drug tolerant proliferative persister (DTPP) cells, were generated by continuous treatment of the respective cell lines with the indicated drug dosage in RPMI-1640 medium (Thermo Fisher Scientific), supplemented with 5% fetal bovine serum (Assaymatrix), 2% L-glutamine (Thermo Fisher Scientific) and 2% Pen/Strep (Thermo Fisher Scientific). Drugs were replenished every 3 days and cells were maintained in the same culture vessel for the whole experiment. The time until the emergence of individual cell states depends on the cell line used, the initial cell number and drug dose. Unless indicated otherwise, WM164 and WM9 cells were exposed to dabrafenib 50 nM 45–55 days, WM164 and WM983b were exposed to dabrafenib 50 nM in combination with trametinib 25 nM for 80–90 days, A375 cells were exposed to vemurafenib 1 μM for 45–55 days, A549 and WM1366 were exposed to docetaxel 5 nM for 45–55 days, HCC827 were exposed to erlotinib 15 nM for 45–55 days and H1975 were exposed to osimertinib 2 nM for 30–35 days to generate IDTC colonies. Similarly, slow-cycling IDTCs were generated using the same drugs for 12–15 days for all cell lines except H1975, which were exposed for 9–12 days. All cells were phenotypically monitored before each experiment to confirm the emergence of the respective phenotype. Lower cell number and higher drug concentrations as well as re-seeding of cells delay the emergence of the IDTC colony phenotype. WM164 and A375 resistant cells were generated by continuous exposure to the respective BRAF inhibitors for 90–120 days. Cells were re-seeded and subjected to 3 weeks (21 days) of drug- free culturing followed by continuous maintenance in the presence of 50 nM dabrafenib.

2.4. Isolating colonies

The colonies were isolated using Pyrex® cloning cylinder 6 mm × 8 mm from Sigma-Aldrich (CLS31666–125EA). The cloning cylinder was placed over the colony and cells were trypsinized for harvesting.

2.5. Metaphase preparation and mFISH Karyotyping

The isolated resistant colony was given 3 weeks of drug holidays followed by two weeks of re-exposure to 100 nM dabrafenib to eliminate the reversible drug tolerant population. Further parent cells and cells isolated from IDTC colony were grown to ~80% confluence and treated with 100 ng/mL Colcemid solution (Gibco) for 4 h, collected by trypsinization and centrifuged at 1000 rpm for 10 min. Cell pellets were re-suspended in 75 mM KCl and incubated for 15 min in a 37 °C water bath. 1/10 vol of 3:1 methanol/acetic acid was added to cells followed by centrifugation at 1000 rpm for 15 min. Cells were then fixed by resuspension in 3:1 methanol/acetic acid solution, incubated for 30 min at room temperature, centrifuged at 1200 rpm for 5 min and finally washed once more with fixative. Cells were re-suspended in a small volume of fixative, dropped onto clean glass slides and let to air dry. Multicolor FISH (mFISH) was performed according to manufacturer's

instructions (MetaSystems) and visualized using the automated Metafer imaging platform (MetaSystems).

2.6. Permutations for the phylogenetic tree

Clustering of cells was performed by extracting cross-over events from the karyograms. Each translocation event was encoded as a binary event. We assumed that two independent cells carrying the same translocation derived one from the other with a shared common ancestor and that de novo generation of the same translocation is a rare and negligible event. In total, we identified 129 presumably independent events (Supplementary Table 1). For ease of plotting, a dummy sample representing a normal diploid genome was added to act as the root of the lineage tree. From these binary properties, the Manhattan-distance between each pair of samples was determined using the "dist" function in R (v3.3.2). The distance matrix was printed in nexus file format and loaded into SplitsTree (v4.14.4) (Huson and Bryant, 2006). Using this software, we generated a Neighbor-Join tree with default settings and plotted it in cladogram style and highlighted the parental cells in bold font. To test the hypothesis that resistance was acquired independently from multiple ancestral cells, we used the following permutation- based approach. For our null-hypothesis we assumed that the average distance between pairs of parental and resistant cells would be roughly equal to the average distance between resistant-resistant pairs. If all resistant cells were derived from the same parental lineage this would manifest itself as a shorter average resistant-resistant distance (XRR) compared to the average resistant-parental distance (XRP) (*i.e.* all resistant are clustered in one branch of the lineage tree). We determined the null-distribution by bootstrapping the distances (without dummy root sample) 50,000-fold and determining the empirical cumulative distribution function (ecdf) of the ratio XRR/XRP. From this distribution we derived that the ratio for the real clustering tree corresponds to a 1-sided p-value of 0.34184. In other words, the resistance was most likely acquired in multiple independent ancestors.

2.7. Sample preparation for metabolomics analysis

For metabolomics analysis parent WM164 cells and all cell states (slow-cycling, colonies and permanent resistant) were cultured and generated on lumox® dish 35 (Sarstedt) in RPMI-1640 medium (Thermo Fisher Scientific), supplemented with 5% fetal bovine serum (Assaymatrix), 2% L-glutamine (Thermo Fisher Scientific) and 2% Pen/Strep (Thermo Fisher Scientific). The same media lot was used for all conditions. Metabolites were extracted 48 h after the last media change by cutting the lumox membrane containing the adherent cells, dip washing it in isotonic 37 °C NaCl supplemented with 2 g/L C13Glucose (Sigma Aldrich) and submerging the whole membrane in 75% EtOH / 25% 1.5 M ammonium acetate solution pre-heated to 85 °C in 15 mL falcon tubes as described previously (Vogel et al., 2019). All steps were performed on a 37 ° heat plate to minimize temperature induced changes. The samples were incubated at 85 °C for 2 min and frozen at − 80 °C until further processing. Cell culture supernatants were collected and centrifuged 1 min, 14,000 rpm at 4 °C. 100 μL of the respective supernatant samples were added to 2 mL of a pre-heated 80% EtOH / 20% 1.875 M ammonium acetate solution, incubated at 85 °C for 2 min and frozen at − 80 °C until further processing. For HPLC-MS analysis, samples were thawed, transferred into fresh 2 mL protein LoBind tubes (Eppendorf) and

dried for 8 h under constant flow of nitrogen at 21 °C. Cell samples were reconstituted in 60 μL, supernatant samples in 100 μL H2O. All samples were centrifuged for 5 min at 14,000 g at 4 °C and transferred into autosampler vials (cells 25 μL, supernatant 25 μL). A small aliquot from each sample was pooled for quality control (QC) with 10 μL from cell samples for cells QC and 15 μL from supernatant samples for supernatant QC. All samples and QC were frozen at − 80 °C. All cell samples were measured in one run, followed by all supernatant samples in a second run. To reduce unwanted metabolite degradation each run was additionally divided into two 24 h batches and only samples for a 24 h batch were freshly thawed and placed into the autosampler at 4 °C.

2.8. Metabolomics measurement of intra- and extracellular metabolites

Samples were measured in a stratified randomized sequence with blanks (MiliQ H2O), QC and ultramix in between. All samples were analyzed with a Dionex Ultimate 3000 HPLC setup (Thermo Fisher Scientific, USA) equipped with a reversed-phase Atlantis T3 C18 pre- and analytical column (Waters, USA) as previously described (Buescher et al., 2010; Vogel et al., 2019). Injection volume was 10 μL and metabolite separation was achieved with a 39-min gradient: 2-propanol was used as eluent A and aqueous methanol solution [(5% methanol v/v), tributylamine (10 mM), acetic acid (15 mM), pH 4.95] was used as eluent B. Mass spectrometric detection was carried out with an LTQ Orbitrap XL system (Thermo Fisher Scientific, USA). Heated electrospray ionization (HESI) was used for negative ionization and masses between 70 and 1100 *m/z* were detected.

2.9. Metabolomics data processing and statistical analysis

Raw data were converted into mzXML by msConvert (ProteoWizard Toolkit v3.0.5) 57, and known metabolites were searched for, with the tool PeakScout (Fröhlich et al., 2016), with a reference list containing accurate mass and retention times. Chromatographic peaks of every substance in every sample were checked manually and peak areas were integrated using the PeakScout software.

Statistical analysis was performed with R [R Core Team] (v3.4.1, packages stats, FactoMineR, missMDA, nlme, lsmeans, readxl, openxlsx) and TibcoSpotfire (v7.6.1). All metabolites were strictly controlled for their analytical quality and graded into two classes, namely suitable for multivariate analysis and univariate analysis (labelled as “MVA_UVA”) only univariate analysis (labelled as “UVA”), or no statistics, only qualitative analysis (only in ultramix, labelled as “no statistics”). Quality was assessed according to the following parameters: difference from target mass, retention time standard deviation, percentage missing values, relative standard deviation in QC, drift with progressing measurement time over run and/or daily batch, blank load in QC. In total, 38 MVA_UVA and 75 UVA intracellular metabolites and 8 MVA_UVA and 103 UVA extracellular metabolites were detected. To correct for cell number differences and to reduce technical variability, median normalization on QC-normalized data was performed. Each metabolite was normalized to the median of the QC value defined as peakareasampleQC-normed = peakareasample/median (peakareaQC). For each sample, the samplemedian was calculated as the median of all peakareasampleQC-normed in the sample and peak areas were normalized as peakareasamplemedian-normalized on QC-normalized data = peakareasampleQC-normed/

samplemedian. Finally, normalized peak areas were log10-transformed. Log10-transformed, normalized data were normally distributed according to the Kolmogorov Smirnov test (99.1% of all metabolites were normally distributed) and homoscedastic according to the Brown-Forsythe Levene-type test (3.5% were significantly heteroscedastic with $p < 0.01$, p-values reported in Supplemental Table 2). For univariate analysis ANOVA was performed with the fixed factor cellular_state (R function lm, aov) and p-values were Benjamini-Hochberg (BH) adjusted (R function p-adjust). All samples were checked for analytical outlier behavior according to the sample median, peak shapes, retention time shifts, percentage of missing values and position in PCA. PCA analysis was performed centered and scaled to unit variance (R function prcomp). Missing values were imputed by a regularized expectation-maximization (R function imputePCA, estim_ncpPCA).

2.10. ChIP and ChIP-qPCR

Chromatin immune precipitation was performed using the Active Motif ChIP-IT® Express Chromatin Immunoprecipitation Kits (53009). WM164 parent, IDTC colonies and dabrafenib resistant cells were fixed using 4% paraformaldehyde for 10 min followed by chromatin preparation according to the manufacturer's protocol. 15 microgram DNA containing chromatin was used as input per reaction. ChIP-grade H3K4me3 (Active Motif Cat: 39159), O-GlcNAc antibody (Active Motif Cat: 61454) or rabbit IgG (Cell Signaling #2729) was used to perform the pulldown. Isolated chromatin was directly used for next generation sequencing or qPCR analysis. Primers (Supplementary Table 4) were used together with SensiFAST™ SYBR® Lo-ROX Kit (Bioline, Bio-94005) for PCR amplification and products were detected by AB7900 Standard real time PCR system (Applied Biosystems).

2.11. ChIP-seq bioinformatics analyses

The ChIP DNA samples were submitted to the Otago Genomics Facility at the University of Otago (Dunedin, New Zealand) for library construction and sequencing. The libraries were prepared using ThruPLEX DNA-seq kit (Takara Bio) according to the manufacturer's protocol. All libraries were uniquely indexed and pooled for single-read sequencing across 8 lanes of HiSeq 2500 High Output, V4 chemistry (Illumina, Inc.), generating 50 bp reads. For data analysis, reads were first trimmed for quality (Phred score >20) and Illumina adapters using fastq-mcf59. Cleaned reads were then aligned to the human genome GRCh37 (hg19) version using BWA60. Alignments were converted to sorted BAM files using SAMtools (1.9) (Li et al., 2009). Peaks were called using Macs2 (2.1.2) callpeak (Feng et al., 2012) on both replicates against both input replicates. ChIP-seq signals were normalized for sequencing depth and effective length using deepTools (2.5.4) (Ramírez et al., 2016). Signal enrichment was checked by plotting the ranked cumulative sum distribution using deepTools.

2.12. ChIP-seq differential peak analysis and annotation

Differential peaks were identified using DESeq2 (Love et al., 2014). Briefly, peak count data were retrieved using featureCounts (Liao et al., 2014). Dispersions were estimated using Generalized Linear Models. Differential events were then defined using Wald test, p-values were adjusted for multiple testing using Benjamini-Hochberg false discovery rate (FDR) <

0.05. Peaks were assigned to the closest gene using Homer66 package (annotatePeaks.pl, v4.9.1). Gene over representation analyses were performed using ReactomePA67 on genes having significant differential peaks (FDR<5%) in their proximal regions as defined by − 5Kb/+ 5Kb from transcription start sites. Only significantly enriched pathways (FDR<5%) were considered. CpGs islands were downloaded from UCSC repository (http://hgdownload.cse.ucsc.edu/goldenpath/hg19/database/cpgIslandExt.txt.gz) and converted to a BED file. Intersections between CpG islands and differentially marked proximal H3K4me3 peaks or universe of peaks (all peaks) were performed using BEDTools intersect (version 2.27.1). Statistical significance was tested using Fisher exact Test using R. Sequence logos for enriched motifs were generated on differential proximal peaks or the overlapping regions between CpG islands and differential proximal peaks using findMotifsGenome.pl tool with the whole genome as background.

2.13. Gene expression analysis

Gene expression analysis were performed as previously described (Ravindran Menon, Das et al. 2015). Briefly, total RNA was labeled using the Ambion WT Expression Kit for Affymetrix GeneChip whole transcript (WT) Expression Arrays® (Life Technologies) and 250 ng of the labeled total RNA was then hybridized to GeneChip Human 1.0 ST arrays according to the manufacturer's instruction. The Affymetrix GeneChip scanner GCS3000 was used for reading. Genomic Suite v6.5 (Partek Inc) was used for the analyses of the results. All samples passed the quality control check and significantly differentially expressed genes were determined using ANOVA. Genes with $p < 0.05$ and FC≥ +/− 1.5 were used for further analysis.

2.14. Immunofluorescence

Cells were fixed with 4% paraformaldehyde (VWR International) for 10 min, washed twice with 1% BSA (Sigma Aldrich) –PBS solution and blocked in 1% BSA/ 5% goat serum/ 0.03% TritonX-100 (Sigma Aldrich) solution for 1 h. Cells were then stained with respective primary antibody (Supplementary Table 5) overnight at 4 °C, washed twice with 1% BSA solution and incubated with the respective secondary antibodies for 3 h. For tumor tissue, frozen sections were OCT (PST-IA018) embedded, cut, and transferred onto glass slides. The slides were fixed for 10 min in 4% paraformaldehyde and washed twice in PBS for 5 min. The cells were permeabilized for 30 min in 0.2% TritonX-100, washed twice with PBS for 5 min each and blocked in 5% goat serum/ 1% BSA/ 0,2% TritonX-100 solution for 1 h. Slides were incubated overnight at 4 °C in primary antibody diluted in blocking solution, followed by two 30 min wash steps in PBS and incubated for 2 h at room temperature with respective secondary antibody in blocking solution. Nuclear counterstaining was performed using Hoechst nuclear stain (Sigma Aldrich) for 20 min. Fluorescence was visualized under an Olympus IX73 microscope and images were analyzed by Image J.

2.15. Live cell imaging

WM164/FUCCI-WM164 cells were maintained in RPMI-1640 medium (Thermo Fisher Scientific), supplemented with 5% fetal bovine serum (Assaymatrix), 2% L-glutamine (Thermo Fisher Scientific) and 2% Pen/Strep (Thermo Fisher Scientific). Cells were maintained in 5% CO2 environment and images were taken with Olympus IX81 microscope.

The image series were overlaid with ImageJ for visualization. Movies depict 4-day treatment periods (Movie S1 and S2).

Supplementary material related to this article can be found online at doi:10.1016/j.drup.2023.100993.

2.16. Xenograft tumor model

All animal experiments were performed in accordance with institutional guidelines (Ethics number: SOM/TRI/197/15/DRC) in C.B-17/IcrHanHsdArcPrkdcscid mice. Animals were inoculated subcutaneously with human WM164 and A549 cells (1×10^6) and treatment was started once tumors reached an approximate volume of 200 mm^3. A mixture of 0.75% hydroxyl methyl cellulose/25% ethanol/10% DMSO was used as vehicle. The respective treatment combinations of dabrafenib (10 mg/kg)/trametinib (0.1 mg/kg) and aspirin (100 mg/kg) were dissolved in vehicle and administered by oral gavage once daily. Docetaxel (15 mg/kg) was dissolved in vehicle and administered by intraperitoneal injection every 7 days. Control groups were administered only with vehicle. The tumor volume was monitored twice weekly. Animals were sacrificed at the end of the experiment or when animal wellbeing was outside the protocol defined ethical limits. The tumorigenic potential of WM164 parent cells or cells exposed to dabrafenib for 45 days (IDTC colonies) and dabrafenib/aspirin for 45 days were tested by subcutaneously injecting 5×10^5 cells into the flanks of C.B-17-scid mice. The tumor volume was monitored twice weekly. Animals were sacrificed at the end of the experiment or when animal wellbeing was outside the protocol defined ethical limits.

2.17. Isolation of cells from tumors

RPMI-1640 medium (Thermo Fisher Scientific), supplemented with 10% fetal bovine serum (Assaymatrix), 2% L-glutamine (Thermo Fisher Scientific), 200 U/mL collagenase type IV (Life Technologies), and 0.6 U/mL dispase (Sigma Aldrich) was used as dissociation buffer. 10 mL cell dissociation buffer was used per 1 g of tumor tissue. Tumors cells were minced into small fragments and incubated in dissociation buffer. The tumor cell suspension was then incubated at 37 °C for 2 h with intermittent vortexing for 1 min every 20 min. The cell suspension was filtered with a 70-μm filter and plated in 6 well plates. Cells were grown in standard media for 3 weeks before experiments.

2.18. Immunoblotting

Protein lysates prepared in RIPA buffer (Sigma-Aldrich) supplemented with 1% protease inhibitor cocktail (Cell Signaling Technology) or nuclear cytoplasmic fractions generated using the Nuclear Extraction Kit (Abcam) according to the manufacturers protocol were used for immunoblotting. The protein concentration was measured using Bradford Protein Assay (BioRad). Proteins were separated on a 6–10% SDS-polyacrylamide gel followed by transfer to a polyvinylidene difluoride membrane (BioRad). The Membrane was then probed for the protein of interest with the specific primary and the corresponding peroxidase conjugated secondary antibodies (Supplementary Table 5). Proteins were visualized using Amersham ECL Select Western Blotting Detection Reagent (GE Healthcare) and scanned on an LI-COR C-DiGit® Blot Scanner. The membranes were stripped and re-probed using

Restore Plus Western Blot stripping buffer (Thermo Fisher Scientific) as required in the individual experiment.

2.19. Immunoprecipitation

Untreated cells or cells at the IDTC colony state were lysed using 1x Cell Lysis Buffer (Cell Signaling) and sonicated on ice three times for 5 s. Cell lysates were subject to a pre-cleaning step by incubating with Protein G Agarose Beads (Cell Signaling) for 1 h at 4°C with gentle rocking. Pre-cleaned cell lysates corresponding to 500 μg total protein were mixed with 2 μL Anti-O-Linked N-Acetylglucosamine antibody [RL2] (Abcam ab2739) and incubated overnight at 4°C with gentle rocking. Immunoprecipitation was performed by adding 10 μL Protein G Agarose Beads (Cell Signaling) per 100 μL cell lysate and incubated for 3 h. Co-immunoprecipitation was then assessed by immunoblotting using specific antibodies for OGT and Histone 3 (Supplementary Table 5).

2.20. RT-qPCR

Total RNAs were isolated using a QIAGEN RNA easy kit according to the manufacturer's protocol and Tetro cDNA synthesis kit (Bioline) was used to generate cDNA. SensiFAST™ SYBR® Lo-ROX Kit (Bio-94005) was used for PCR amplification and products were detected by AB7900 Standard real time PCR system (Applied Biosystems). ACTB was used as housekeeping genes and relative gene expression levels were calculated using the ddCT method. Primers are summarized in Supplementary Table 4.

2.21. Crystal violet staining

At the end of the respective experiments, cells were fixed with 4% paraformaldehyde, followed by 30 min incubation with 0.05% crystal violet solution. The plates were then washed, air dried at room temperature and scanned using BioRad Gel Doc.

2.22. shRNA transduction and lentiviral vectors

shPRKAA1 (TRCN0000000861), shPRKAA2 (TRCN0000002171), shOGT (TRCN0000293652) and shTET1 (TRCN0000075024) were ordered from Sigma Aldrich. Transduction were carried out according to the manufacturer's protocol. Briefly cells were incubated with 8 ng/mL polybrene complete media and incubated overnight with the lentiviral particles and selected by exposing the cells to 5 μg/mL puromycin for 2 weeks. WM164 GFP and RFP driven with EF1alpha promoter were generated as previously reported (Škalamera et al., 2012). Fluorescent cells were sorted 72 h after transduction using MoFlo® Astrios™ cell sorter.

2.23. MTT assay

2 × 104 cells were seeded in 96-well culture plates and exposed to the respective experimental conditions. At the end of the experiment, MTT (3-(4, 5-dimethylthiazolyl-2)–2,5diphenyltetrazolium bromide) assay (Thermo Fischer Scientific) was performed according to the manufacturers protocol. Briefly, cells were exposed to 1.2 mM MTT solution in culture media at 37°C for 4 h. After incubation, 85 μL MTT solution were removed and MTT reagent was dissolved in 50 μL DMSO, incubated at 37 °C for 10 min

before absorbance was measured at 540 nm using a microplate reader. All experiments were performed in triplicate.

2.24. Statistical analysis

Statistical analysis was performed using GraphPad Prism 8. Data are represented as arithmetic mean + /− standard deviation. Unpaired two-tailed t-test or ANOVA has been performed. If indicated, correction for multiple testing was performed using the Holm-Sidak method. N.s. indicates a P value > 0.05, * indicates a P value ≤ 0.05, * * indicates a P value ≤ 0.01, * ** indicates a P value ≤ 0.001, and * ** * indicates a P value ≤ 0.0001. No statistical methods were used to predetermine sample sizes. Pearson's correlation was calculated in python (v3.10) using pandas (v1.9). Details about statistical analysis of metabolomics and ChIP-sequencing are summarized in the respective sections.

3. Results

3.1. Continuous drug exposure identifies intermediate phenotypic cell states, preceding permanent acquired drug resistance

Based on our previous work describing a slow-cycling multidrug-tolerant cell state, termed induced drug-tolerant cells (IDTCs) (Ravindran Menon, Das et al. 2015), which resemble DTPs (Ramirez, Rajaram et al. 2016, Hong, Moriceau et al. 2018) we exposed melanoma cells to the BRAF inhibitor dabrafenib and monitored cell cycle characteristics over time using the fluorescent ubiquitination-based cell cycle indicator (FUCCI) system that allows real time assessment of the cell cycle (Sakaue-Sawano, Kurokawa et al. 2008). BRAF inhibitor treatment leads to cell cycle arrest in the G1 phase with the development of IDTCs, characterized by increased expression of NGFR, as previously reported (Ravindran Menon, Das et al. 2015) (Figs. 1a, (2); Supplementary Fig. 1a). Despite continuous drug exposure, individual cells eventually escaped the slow-cycling IDTC state, regained proliferative capacity and formed proliferating cell clusters called IDTC colonies, resembling DTPPs (Ramirez, Rajaram et al. 2016, Hong, Moriceau et al. 2018) (Figs. 1a, (3)). Cells outside these colonies remained slowly cycling (Figs. 1a, (3)). Interestingly, the IDTC colony phenotype developed also by cell migration (Movie S1, S2), suggesting an important function of cell mobility for early cluster formation. Eventually, colonies dispersed and gave rise to a cell population with the same cell cycle characteristics as untreated parental cells, in the presence of drugs, signifying the development of acquired drug resistance as previously reported (Ravindran Menon et al., 2015) (Fig. 1a (4 and 5)). The number of IDTC colonies peaked around 50 days after treatment initiation before decreasing and disappearing (Fig. 1b) and did not correlate with cell proliferation, which gradually increased over time (Fig. 1c). Accordingly, NGFR expression was increased in IDTCs and IDTC colonies but disappeared in resistant cells (Supplementary Fig. 1a). The IDTC colony phenotype was also observed following exposure to different anti-cancer agents in different cancer types (Supplementary Fig 1. b–e), highlighting the prevalence of this phenomenon. Because of the transient nature of the IDTC colony phenotype and the reversibility of the early slow-cycling IDTC state (Ravindran Menon, Das et al. 2015, Emran et al., 2018), we hypothesized that the IDTC colony state may also represent a reversible drug resistant cell state. To test reversibility of drug resistance, WM164 cells isolated after 45 and 65 days

of BRAF inhibitor treatment were subjected to 21 days of drug holiday and re-challenged with BRAF inhibitors. The results were compared to WM164 parent and WM164 BRAF inhibitor resistant (90 days treated) cells exposed to BRAF inhibitor (Fig. 1d). We observed that 45 days treated cells did not show any signs of resistance while 65 days treated cells showed partial resistance to BRAF inhibitors. We hypothesized that the densely packed cell structures of IDTC colonies are specifically important for the re-initiation of proliferation. To test this hypothesis, we investigated reversibility of drug resistance in isolated IDTC colonies rather than the entire population. We found that WM164 IDTC colonies start dispersing after 75 days of drug exposure, suggesting a gradual process (Supplementary Fig. 1f). Hence, WM164 IDTC colonies isolated after 45, 55, 65 and 75 days of BRAF inhibitor exposure were subjected to 21 days drug holidays and re-challenged with BRAF inhibitor (Fig. 1e). 75 days BRAF inhibitor treated WM164 cells outside the colonies were isolated and subjected to the same treatment as controls (Fig. 1f). Re-challenged cells in the early IDTC colony state (45 and 55 days) completely re-gained drug sensitivity (Fig. 1e) while, IDTC colonies treated for 65 days showed partial drug resistance and 75 days treated colonies showed near complete resistance to BRAF inhibitor (Fig. 1e), indicating a gradual stabilization of the resistant phenotype. In comparison, cells surrounding IDTC colonies remaining in the slow-cycling state after 75 days of treatment completely regained drug sensitivity following drug holidays (Fig. 1f). The cell cycle characteristics of cells in IDTC colonies readily responded to drug withdrawal or re-treatment (Supplementary Fig. 2), suggesting no fitness disadvantage and subsequent selection pressure in the absence of drug(s). Overall, the data show a multi-state adaptive response of cancer cells to drug treatment, initially involving reversible cellular reprogramming that is eventually stabilized over time (Fig. 1g). The time frame of this progression *in vitro* appears to be partially dependent on the cytotoxicity level of the initial treatment as addition of MEK inhibitors to BRAF inhibitors delays the formation of the colony phenotype (Supplementary Fig. 1e). To investigate the origin of the cells forming the IDTC colonies we co-cultured GFP- and RFP-expressing WM164 cells in a 1:1 ratio and exposed them to dabrafenib. The resulting distribution of approximately 25%/25%/50% of GFP-only, RFP-only and double-positive IDTC colonies (Fig. 1h) indicates IDTC colonies are predominantly multi-clonal. To substantiate these results, we performed whole chromosome painting (mFISH) in untreated parental cells and cells isolated from IDTC colonies after 75 days of treatment. The cells showed a considerable amount of heterogeneity regarding chromosomal re-arrangements and a phylogenetic tree generated based on identified signature chromosomal aberrations (Supplementary Table 1). Multiple resistant clones were more closely related to different parental clones, suggesting a multi-clonal origin of the cells forming a single IDTC colony (Fig. 1i).

3.2. H3K4me3 remodeling during the development of permanent acquired drug resistance

Previous reports including ours have shown that formation of persisters/IDTCs in multiple cancers are characterized by the downregulation of histone3 lysine 4 trimethylation (H3K4me3) (Ravindran Menon, Das et al. 2015, Emran et al., 2018, Shaffer, Dunagin et al. 2017). Hence, H3K4me3 levels in early IDTCs and after colony formation were monitored in multiple cancer cell lines treated with BRAF inhibitor (WM164 and A375), EGFR

inhibitor (H1975) and Docetaxel (A549) (Fig. 2a). We observed a considerable increase in H3K4me3 levels in IDTC colony samples in comparison to 15 days treated samples. In WM164 and A375 90 days treated BRAF inhibitor resistant cells H3K4me3 levels remained stabilized (Fig. 2a). Immunofluorescence images of H3K4me3 showed that cells displaying the IDTC colony morphology show a strong H3K4me3 signal (Supplementary Fig. 3a). To investigate the molecular consequences of H3K4me3 remodeling during the development of acquired drug resistance, chromatin immunoprecipitation followed by high throughput sequencing (ChIP-seq) was performed in untreated parental cells, IDTC colony and dabrafenib-resistant cells. The ChIP seq experiment resulted in 32,322 peaks in untreated parental cells, 22,854 in IDTC colony and 20,087 in dabrafenib-resistant cells. Differential expression analysis showed extensive H3K4me3 remodeling, with 7212 and 9786 differentially marked peaks in colonies and resistant compared to parental cells, respectively (Supplementary Fig 3b). ChIP-qPCR using H3K4me3-specific negative and positive primer sets (Supplementary Fig. 3c) and the characteristic global H3K4me3 distribution around transcription start sites (TSS) (Fig. 2b) confirmed the specificity of the ChIP experiment. Peaks in proximity of TSS (−5Kb/+5Kb) encompassed the majority (5165/7212 and 7249/9786) of differentially marked peaks (Supplementary Fig. 3d) and corresponded to 4766 and 6548 genes in parent compared to IDTC colony or resistant cells, respectively. Pathway enrichment analysis of these genes showed activation of cellular response to stress, WNT signaling related pathways, SUMOylation related pathways and pathways related to epigenetic regulation as most strongly affected by H3K4me3 remodeling, while genes involved in pathways related to cell cycle regulation, p53 signaling and Rho GTPase signaling showed decreased H3K4me3 marking (Fig. 2c). Alterations of global SUMOylation and transient accumulation of active β-catenin were confirmed during the development of permanent drug resistance (Supplementary Fig. 3e and f). The observed transient accumulation of active β-catenin in slow cycling IDTCs and the continuous H3K4me3 remodeling in WNT signaling related pathways indicates the initiation of a permissive epigenetic state at β-catenin target genes early in the development of permanent drug resistance and is reminiscent of H3K4me3 remodeling following transient activation of β-catenin during senescence-associated reprogramming of cancer cells (Milanovic, Fan et al. 2018). Comparing genes with differential H3K4me3 markings with differentially expressed genes in microarray data of WM164 cells treated with the BRAF inhibitor Vemurafenib for 60 days showed a positive correlation of H3K4me3 markings with gene expression (Pearson’s correlation 0.42), supporting the functional relevance of the observed epigenetic remodeling (Fig. 2d). The pathway enrichment analysis of differentially marked genes showed substantial overlap between the top enriched pathways in IDTC colony *vs* parent and resistant *vs* parent. In fact, ~47% genes with increased H3K4me3 in IDTC colony compared to parent cells also show increased H3K4me3 markings in resistant compared to parent cells. Similarly, ~37% of genes with decreased H3K4me3 marking in IDTC colony compared to parent cells also show decreased H3K4me3 markings in resistant compared to parent cells, suggesting a gradual stabilization of some epigenetic markings (Fig. 2e). Despite the high similarity of the IDTC colony and resistant ChIP-seq datasets, a direct comparison of IDTC colony and resistant cells showed 3488 decreased and 5503 increased differentially marked H3K4me3 peaks in resistant compared to IDTC colony (Supplementary Fig. 4a). Pathway enrichment analysis showed that IDTC colonies have

increased H3K4me3 in pathways related to Rho GTPase signaling, cell cycle progression, RUNX2 signaling and the circadian clock while showing decreased H3K4me3 in pathways related to kinase signaling and metabolism compared to resistant cells (Supplementary Fig. 4b), suggesting gradual epigenetically regulated adaption at later stages of the development of acquired drug resistance.

3.3. Therapy induced H3K4me3 remodeling preferentially occurs at CpG island motifs

Motif analysis of H3K4me3 peaks was performed to identify possible transcription factors associated with epigenetic remodeling. ELK1, ARNT, ELK4, ELF1 and FLI1 were identified as the 5 commonly enriched DNA sequences within the top 20 enriched DNA sequences in IDTC colony and resistant, but not parent cells (Fig. 3a, Supplementary Table 3). Further analysis of top 20 enriched DNA sequences in differentially regulated H3K4me3 motifs between all conditions revealed MYB, BMYB, FLI1, ELK1, ELK4, ETV2 and RFX6 as the 7 commonly enriched DNA sequences (Fig. 3b, Supplementary Table 3), suggesting prominent accumulation of H3K4me3 in areas of the ELK1, ELK4 and FLI1 DNA binding motifs. Analysis of differential H3K4me3 peaks of parent and IDTC colonies revealed that most epigenetic changes occurred at CPG island regions. Differentially marked proximal H3K4me3 peaks between parent and IDTC colony or resistant showed an 82% (4228/5165) and 88% (6361/7249) overlap with CpG islands, indicating preferential remodeling of H3K4me3 associated with CpG islands (Figs. 3c and 3d). ELK4, ELK1, FLI1, ELF1 and ETS were identified as the top 5 enriched DNA sequences within CPG island regions of the differentially marked H3k4me3 peaks of both parent *vs* IDTC colony and parent *vs* resistant comparison.

Next, we tested the expression of 21 genes that have previously been linked to acquired drug resistance (Shaffer, Dunagin et al. 2017). Of the resistance associated genes, 52% (11/21) showed changes of H3K4me3 peaks closest to their TSS with strong correlation (Pearson's correlation >0.95) between expression (log2FC as determined by RT-qPCR) and H3K4me3 markings (log2FC of H3k4me3 as determined by ChIP-seq) (Fig. 3e). Of all genes with differentially expressed H3K4me3, 73% (8/11) showed significant changes of their gene expression (2 are downregulated and 6 are upregulated in the IDTC colony state) (Fig. 3e and Supplementary Fig. 5a). Of the upregulated genes that also show increased H3K4me3 in IDTC colonies compared to parent cells, 83% (5/6) showed H3K4me3 remodeling overlapping with CpG islands (Fig. 3e and Supplementary Fig. 5a), suggesting a prominent role of CpG island specific H3K4me3 remodeling for their regulation. We picked *EGFR, CDH2* (upregulated and marked) and *PDGFRB* (upregulated not marked) to confirm H3K4me3 enrichment using ChIP qPCR (Supplementary Fig. 5b and c), further underscoring the specificity of our ChIP experiments.

Taken together, H3K4me3 ChIP-seq of the different states of drug-induced cellular reprogramming showed extensive, partially stabilized epigenetic remodeling, preferentially at genes harboring CpG islands and a limited set of TF DNA binding consensus motifs including ELK1 and ELK4. Genes are involved in multiple pathways implicated in BRAF inhibitor resistance and appear regulated by H3K4me3 remodeling exemplifying the relevance of this process for the development of acquired drug resistance.

3.4. Transiently resistant IDTC-colonies upregulate H3K4me3 through O-linked N-acetylglucosamine transferase

We next decided to focus on the molecular logic of early remodeling of H3K4me3 in IDTC colonies. Because the analysis of H3K4me3 differentially marked peaks in CPG island regions revealed ELK1 and ELK4 TF binding sequences to be the top candidates, we tried to understand how ELK1 and ELK4 could be related to H3K4me3 remodeling. We could not find any relevant literature that linked ELK1 and ELK4 to H3K4me3 upregulation. We also did not see any significant increase in ELK1 or ELK4 expression at the IDTC colony state (Supplementary Fig. 5d). However, ELK1 and ELK4 DNA binding motifs have recently been described to be enriched in O-GlcNAc marked chromatin (Itkonen, Urbanucci et al. 2019) and we were able to confirm O-GlcNAc markings in selected resistance associated genes (Supplementary Fig. 5e). OGT is the only protein that catalyze the addition of single ring sugar, O-GlcNAc, to serine and threonine residues to modify their function, stability, and localization (Fardini, Dehennaut et al. 2013, Chiaradonna, Ricciardiello et al. 2018). Importantly, OGT has been reported to regulate SET1/COMPASS mediated H3K4me3 remodeling (Deplus, Delatte et al. 2013). In addition, it has been shown to function closely with TET1 protein to regulate H3K4me3 marks in embryonic stem cells. TET1 helps in the recruitment of OGT to chromatin (Deplus, Delatte et al. 2013). OGT and TET1 co-localize with H3K4me3 peaks at unmethylated CpG-rich promoters (Vella, Scelfo et al. 2013). Hence, we hypothesized that OGT and TET1 could be involved in the H3K4me3 remodeling process. We observed that OGT and TET1 protein and mRNA levels were upregulated at the IDTC colony state (Fig. 4a and Supplementary Fig. 6a). Isolated individual IDTC colonies showed an upregulation of both OGT and TET1 mRNA levels (Supplementary Fig. 6b). Accordingly, an increase in O-GlcNAcylation levels at the IDTC colony state was found confirming increased OGT catalytic activity (Fig. 4b). The O-GlcNAcylation levels were also increased in the nuclear fraction of the IDTC colony state (Supplementary Fig. 6c). In contrast, expression of OGT and TET1 were not consistently increased at the slow-cycling IDTC state (Fig. 4a and Supplementary Fig. 6d), suggesting state specific expression of these enzymes corresponding to H3K4me3 levels (Fig. 2a). Previously reported melanoma patient derived xenograft models after 30 days of treatment with the MEK inhibitor TAK-733 (Micel, Tentler et al. 2015), a time point corresponding to the IDTC colony state showed increased OGT, TET1 and O-GlcNAcylation in the majority of samples, irrespective of the mutational background (Fig. 4c).

OGT activity is reported to be fueled by the hexosamine biosynthesis pathway (HBP) (Akella, Ciraku et al. 2019). Metabolomics analysis of WM164 parental, IDTC, IDTC colony state and 90 days treated resistant cells for 113 intracellular components including amino acids, fatty acids, intermediates of glycolysis and the citric acid cycle allowed a broad overview of the cellular metabolic profile (Supplementary Table 2). Detailed investigation of the metabolomics data showed that the HBP was significantly activated at the IDTC colony state as evidenced by increased levels of its end product UDP-N-acetylglucosamine as well as all detected metabolites feeding into this pathway (Figs. 4d and 4e). UDP-N-acetylglucosamine acts as the substrate for O-GlcNAcylation catalyzed by OGT. Principle component analysis revealed that untreated parental cells and permanent resistant cells in the presence of drug(s) clustered together, while cells in the slow-cycling IDTC state or the

re-proliferative IDTC colony state clustered separately, suggesting distinct metabolic states (Supplementary Fig. 6e). Similarly, principal component analysis of secreted components in the conditioned media showed distinct clustering of each state (Supplementary Fig. 6f).

Furthermore, immunoprecipitation revealed increased O-GlcNAcylation of histone 3, a known OGT target (Fong, Nguyen et al. 2012), suggesting increased OGT-mediated epigenetic modifications at the IDTC colony state. It's noteworthy that increased O-GlcNAcylation of histone 3 is evident in all cell lines despite clear cell line dependent effects of both baseline and drug induced O-GlcNAcylation levels. (Fig. 4f). Inhibition of OGT by OSMI4B (Martin, Tan et al. 2018), a recently developed cell-penetrating OGT inhibitor for *in vitro* studies, efficiently downregulated H3K4me3 levels at the IDTC colony state confirming the role of OGT in H3K4me3 remodeling (Fig. 4g). Inhibition of OGT also downregulated the expression of BRAF inhibitor resistance associated genes like NRG1, WNT5A, VEGFC and EGFR at the IDTC colony state which were also associated with H3K4me3 remodeling (Fig. 4h). However, FGFR1, RUNX2, JUN and CDH2 did not show any significant downregulation suggesting OGT independent mechanisms (Supplementary Fig. 6g). AXL and IGF2 genes related to BRAF inhibitor resistance but unassociated with H3K4me3 remodeling were also downregulated in IDTC colony state after OGT inhibition, suggesting potential indirect or H3K4me3 independent effects of OGT in BRAF inhibitor resistance (Supplementary Fig. 6h). Furthermore, expression levels of transcription factors FLI1 and ARNT that showed motif enrichment in our H3K4me3 ChIP-seq data also showed dependence on OGT (Supplementary Fig. 6i), suggesting direct and indirect effects of OGT on H3K4me3 remodeling. ELF1 transcript levels did not depend on OGT and did not show any significant difference in any of the conditions tested (Supplementary Fig. 6i). Together the data suggest an important role for OGT in H3K4me3 remodeling and the acquired resistance phenotype at the IDTC colony state.

3.5. Inhibition of OGT blocks therapy-induced cellular reprogramming preventing tumor recurrence

To determine the functional relevance of OGT for therapy-induced reprogramming, we generated shRNA mediated OGT knockdown cell lines (Fig. 5a). Knockdown of OGT did not decrease growth rate (Supplementary Fig. 7a) or sensitize cells for short-term treatment (Supplementary Fig. 7b) *in vitro*. However, shOGT cell lines showed a markedly decreased ability to form IDTC colonies compared to shControl cells (Fig. 5a) following prolonged drug exposure. We observed similar effects when cells were treated with the OGT inhibitor OSMI4B (Supplementary Fig. 7c) or Benzyl-N-acetyl-α-galactosaminide (BADG) (Supplementary Fig. 7d). In contrast to OGT inhibition, the OGA inhibitor PUGNAc that stabilizes pre-existing O-GlcNAc modification, rather than inducing O-GlcNAc in new target proteins, did not affect colony formation (Supplementary Fig. 7d) despite increasing global O-GlcNAc levels (Supplementary Fig. 7e). In line with the reported functions of TET proteins for OGT stability and chromatin localization (Deplus, Delatte et al. 2013, Vella, Scelfo et al. 2013, Ito, Katsura et al. 2014), knockdown of TET1 did not consistently affect the growth rate or drug sensitivity (Supplementary Fig. 7f and g) but decreased the efficiency of therapy induced IDTC colony formation (Fig. 5b). Sparse IDTC colonies that formed during long term BRAF inhibitor exposure in shOGT cell populations showed that

OGT transcript levels were re-activated compared to the whole cell population, highlighting the importance of OGT for the formation of this phenotype (Supplementary Fig. 7h).

Regain of H3K4me3 and increased OGT and TET1 expression were absent in chronically treated shOGT and shTET1 cells compared to shControl cells (Supplementary Fig. 7i and 7j). Like *in vitro* results, shOGT and shTET1 cells showed no growth differences *in vivo* compared to shControl but displayed prolonged response to BRAF/MEK inhibition, resulting in significantly decreased tumor burden compared to shControl mice (Fig. 5c). Immunoblotting showed that OGT, TET1 and O-GlcNAc levels were all increased in the treated shControl tumors, which was diminished in the treated shOGT tumors (Fig. 5d). Immunofluorescence revealed that H3K4me3 levels remained low in the BRAF/MEK inhibitor treated shOGT and shTET1 tumors compared with shControl (Fig. 5e). The importance of OGT *in vivo* was also confirmed in a lung adenocarcinoma xenograft model using KRAS mutant A549 cells treated with weekly intraperitoneal injected docetaxel (Fig. 5f). Altogether, the data shows that OGT and TET1 play key roles during the emergence of acquired drug resistance by enabling cancer cells to regain proliferative capacity.

3.6. AMP-activated protein kinase (AMPK) activation prevents OGT-mediated cellular reprogramming

Despite ongoing efforts, the development of specific OGT inhibitors for *in vivo* use has not yet been successful (Trapannone et al. 2016, Martin et al. 2018). OSMI-4b (Martin et al. 2018) inhibits global O-GlcNAc and IDTC colony formation in our *in vitro* model. Due to limited *in vivo* data available for this novel inhibitor, we decided to explore indirect ways to inhibit OGT function. Recent reports show that AMPK is able to prevent O-GlcNAcylation by decreasing HBP flux (Gelinas et al. 2018), interfering with OGT chromatin binding (Xu et al. 2014) and direct regulation of OGT in an mTOR-dependent manner (Sodi, Khaku et al. 2015). Accordingly, combination of anti-cancer drugs with the AMPK activator aspirin prevented IDTC colony formation compared to single treatment (Fig. 6a). Furthermore, the combination of dabrafenib with either aspirin or another AMPK activator, metformin, inhibited the re-activation of cell proliferation that is typically seen between 45 and 80 days in WM164 melanoma cells (Fig. 6b). WM164 cells treated with the combination of dabrafenib, and aspirin for 235 days regained drug sensitivity following 21 days of drug holidays (Fig. 6c), indicating the prevention of permanent drug resistance. Aspirin combination treatment for 45 days induced phosphorylation of the AMPK target acetyl-CoA carboxylase (p-ACC) and inhibited drug-induced increase of OGT and O-GlcNAcylation (Fig. 6d) as well as re-activation of H3K4me3 (Fig. 6e). OGT transcript levels were also found to be decreased in multiple cell lines after chronic treatment of aspirin in combination with different chemotherapeutic drugs (Supplementary Fig. 8a), confirming AMPK activation as a suitable strategy to interfere with therapy-induced OGT expression. The effect of aspirin in long term treatments was not due to synergy between the drugs as short-term combination showed no increased cytotoxicity (Supplementary Fig. 8b). ShRNA-mediated gene knockdown of the catalytic subunits AMPKα1/2 (*PRKAA1/PRKAA2*) (Supplementary Fig. 8c) abrogated the aspirin-mediated H3K4me3 downregulation and resulted in the emergence of IDTC colonies even in the presence of Aspirin (Fig. 6f, Supplementary Fig. 8d). Similarly, the triple combination of cell type specific drug(s),

aspirin and the AMPK inhibitor dorsomorphin (Compound C), rendered aspirin ineffective in preventing the re-activation of H3K4me3 (Supplementary Fig. 8e), confirming the potential of AMPK to block therapy-induced epigenetic reprogramming.

These experiments were extended to melanoma xenografts to test the combination of BRAF/MEK inhibitor treatment with aspirin *in vivo*. In line with the *in vitro* results, aspirin alone did not affect tumor growth, but combined dabrafenib/trametinib/aspirin showed a prolonged response compared to dabrafenib/trametinib, which started to relapse after approximately 19–21 days of treatment, resulting in a significant difference of tumor volume at the end of the experiment (Fig. 6g). Immunoblotting and immunofluorescence staining of tumor sections showed time-dependent changes of OGT, TET1 and H3K4me3 that resembled our *in vitro* findings of diminished OGT, O-GlcNAc and H3K4me3 in tumors treated with the dabrafenib/trametinib/aspirin triple combination (Figs. 6h and 6i), suggesting that aspirin can block therapy-induced metabolic and epigenetic reprogramming *in vivo*.

We have previously reported high initiating potential of early IDTCs (Ravindran Menon, Das et al. 2015). Therefore, the tumor-initiating potential of WM164 cells at the IDTC colony state and the effects of chronic treatment combined with aspirin was tested. WM164 cells exposed to dabrafenib (IDTC colony state) for 50 days *in vitro* showed significantly increased *in vivo* growth potential compared to untreated parental cells, which was prevented by aspirin co-treatment (Supplementary Fig. 8f). Cells isolated from tumors and subjected to drug holidays *in vitro* regained drug sensitivity for all conditions (Supplementary Fig. 8g), indicating that transient epigenetic reprogramming is sufficient to induce disease relapse. Altogether, we identified AMPK as an actionable target to interfere with OGT-mediated development of acquired drug resistance.

4. Discussion

Evidence is mounting that a cell-intrinsic adaptive response is a major contributor to acquired drug resistance in different cancer types and treatment regimens (Shaffer et al. 2017, Hammerlindl and Schaider, 2018, Bai et al. 2019). Reversible epigenetic remodeling in a slow cycling persister phenotype, has been first reported more than a decade ago as the immediate response to drug treatment (Sharma et al. 2010). Based on our previous work in which we described this persister phenotype as an innate stress response that leads to slow-cycling induced drug tolerant cells (IDTCs) (Ravindran Menon et al. 2015), we have expanded this model to chronic drug treatment and identified a re-proliferative colony phenotype (IDTC colony) as the missing link to stable drug resistance. Similar to early IDTCs (Ravindran Menon et al. 2015), IDTC colonies are not the result of pre-existing subpopulations that are enriched during prolonged drug treatment but represent a dynamically regulated intermediate state that initially remains reversible. The IDTC model, specifically the identified $NGFR^{high}$ IDTC colonies resemble findings of minimal residual disease (MRD) that show a “starved” cellular phenotype with low metabolic activity after treatment initiation, followed by a transition towards a $NGFR^{high}$ stem-like state (Rambow et al., 2018). This $NGFR^{high}$ subpopulation has been found to cluster together and drive tumour relapse (Rambow et al., 2018), highlighting the importance of phenotypic

conversions *in vivo*. We observed that cell migration is contributing to the development of the cluster morphology and our H3K4me3 ChIP seq experiments showed that genes associated with Rho GTPase signaling undergo H3K4me3 remodeling in colony *vs* parent as well as colony *vs* resistant cells. While the importance and molecular mechanism of cell migration involved in IDTC colony formation remains to be uncovered, our studies hint at a potential involvement of Rho GTPase signaling.

Our four-state model is in line with recently described multi-stage differentiation subtypes in melanoma cells and patients in response to MAPK pathway inhibition or immune therapy (Tsoi et al., 2018, Bai et al., 2019) and resembles resistance emerging from dynamic transcriptional heterogeneity in melanoma and other cancer types (Shaffer et al., 2017), supporting the broad applicability of the described therapy-induced cellular reprogramming model.

Previous studies have underlined the importance of losing H3K4me3 in the early persister phenotype. Downregulation of multiple pathways is necessary for maintaining the dormant phenotype aided by downregulation of H3K4me3, an active chromatin mark. Accordingly, our studies indicate that escape of cancer persisters from the dormant state is instigated by the regain of H3K4me3. In WM164 cells treated with BRAF inhibitor, H3K4me3 upregulation in IDTC colonies correlated with upregulation of multiple genes reported to cause BRAF/MEK inhibitor resistance. H3K4me3 ChiP Seq revealed that the majority of H3K4me3 remodeling occurred at CPG island regions. Motif analysis of differentially regulated H3K4me3 peaks identified OGT consensus DNA binding motifs ELK1 and ELK4 (Itkonen et al., 2019) among the top 5 modified regions in IDTC colonies and resistant cells compared to parental cells. OGT, together with TET1, is a key player of the adaptive H3K4me3 remodeling process, supported by previously reported functions of these genes in embryonic stem cells (Deplus et al., 2013, Vella et al., 2013, Wu et al., 2017). TET1 plays an important role recruiting OGT to chromatin (Vella, Scelfo et al. 2013) and initiating DNA demethylation at CpG island regions (Tahiliani et al., 2009). It co-localizes with H3K4me3 peaks at TSS (Vella et al., 2013). Binding of OGT to TET1 is also known to enhance its functions (Hrit et al., 2018). Metabolic characterization of the individual cell states during transition to acquired drug resistance revealed the upregulation of the hexosamine biosynthesis pathway which generates the necessary substrate for OGT activity. Accordingly, O-GlcNAc ChIP qPCR showed an increase in O-GlcNAc modification in promoters of genes EGFR and CDH2 associated with H3K4me3 remodeling. PDGFRB gene which did not show any differences in H3K4me3 peak also showed an upregulation of O-GlcNAc modification in its promoter. These results suggest that OGT binding to chromatin may not always lead to H3K4me3 remodeling and could be dependent on the binding of other factors like TET1.

Inhibition of OGT reduced H3K4me3 levels, and the expression of genes associated with BRAF/MEK inhibitor resistance. Knockdown of both OGT and TET1 inhibited the formation of IDTC colonies *in vitro* and delayed acquired drug resistance *in vivo.* This epigenetic adaptive process can also be blocked indirectly through forced activation of AMPK which downregulated OGT expression and activity. AMPK activators have been previously proposed to synergize with BRAF inhibition and delay the development of

BRAF inhibitor resistance (Yuan et al., 2013). We now show that the effectiveness of AMPK-activating drugs goes beyond cytotoxic synergy by blocking the adaptive cellular reprogramming process that drives tumor relapse, which may be linked to the observed survival benefit of post-diagnosis aspirin use in melanoma patients (Rachidi, et al., 2018). While our studies cannot exclude OGT independent effects of AMPK activation that contribute to the delayed development of drug resistance, our results, supported by several studies showing direct interactions of AMPK and OGT (reviewed in Gelinas et al., 2018), suggest an important role for the AMPK-OGT axis for this process. These observations are in line with reports that suggest OGT expression with poor prognosis (Gao et al., 2018, Lin et al., 2018) and link O-GlcNAc modified transcription factors with genotoxic stress response in cancer (Liu et al., 2020).

Together, co-targeting oncogenic drivers and mediators of stress-induced cellular reprogramming like OGT could trap cells in a slow-cycling persister state, preventing the development of permanent acquired drug resistance and disease relapse. The vulnerabilities of cancer persisters could then be either directly targeted (Zou et al., 2019, Sun et al., 2022) or the reversibility of the phenotype could be exploited through scheduled treatment interruption and re-challenge (Schreuer et al., 2017). While the mechanistic details of the epigenetic reprogramming and stabilization as well as the specific contribution of the OGT/TET1/H3K4me3 complex-mediated transcriptional programs remain to be elucidated, this work identified a novel mechanism of epigenetic reprogramming that can be targeted to inhibit cancer plasticity and adaption, ultimately prolonging treatment success of current standard of care.

Supplementary Material

Refer to Web version on PubMed Central for supplementary material.

Acknowledgements

This work was funded by a Research Project Grant awarded by Cancer Council Queensland (APP1163520), the Epiderm Foundation, the Princess Alexandra Hospital Research Foundation (PARSS2016_NearMiss), the Australian Skin and Skin Cancer Research Centre through the ASSC Enabling Grant Scheme and the Meehan Project Grant 021174 2017002565. A.A.E. is funded by The University of Queensland International Scholarship (UQI); H.H. is funded by the International Postgraduate Research Scholarship (IPRS) and UQ Centennial Scholarship (UQCent). We thank Dr Atsushi Miyawaki, RIKEN, Wako-city, Japan, for providing FUCCI constructs. The FUCCI work was supported by project grant APP1084893 (National Health and Medical Research Council) to N.K.H. Work in the G.R. lab is supported by NRF Investigatorship (NRFI05–2019-0008) to GR. Work in the M.R.E. lab is funded by the New Zealand Institute for Cancer Research Trust. Work in the M.F. lab was supported by an NIH/NCI R01CA197919 and Veterans Affairs Merit Review Award 5I01BX001228. This work was further supported by the Cancer League of Colorado, Inc. research grant (AWD-232415) awarded to D.R.M and M.F. This research was carried out at the Translational Research Institute, Woolloongabba, Qld 4102, Australia. The Translational Research Institute is supported by a grant from the Australian Government.

References

Ahronian LG, Sennott EM, Van Allen EM, Wagle N, Kwak EL, Faris JE, Godfrey JT, Nishimura K, Lynch KD, Mermel CH, Lockerman EL, Kalsy A, Gurski JM Jr., Bahl S, Anderka K, Green LM, Lennon NJ, Huynh TG, Mino-Kenudson M, Getz G, Dias-Santagata D, Iafrate AJ, Engelman JA, Garraway LA, Corcoran RB, 2015. Clinical acquired resistance to RAF inhibitor combinations in BRAF-mutant colorectal cancer through MAPK pathway alterations. Cancer Discov. 5 (4), 358–367. [PubMed: 25673644]

Akella NM, Ciraku L, Reginato MJ, 2019. Fueling the fire: emerging role of the hexosamine biosynthetic pathway in cancer. BMC Biol. 17 (1), 52. [PubMed: 31272438]

Bai X, Fisher DE, Flaherty KT, 2019. Cell-state dynamics and therapeutic resistance in melanoma from the perspective of MITF and IFNγ pathways. Nat. Rev. Clin. Oncol. 16 (9), 549–562. [PubMed: 30967646]

Buescher JM, Moco S, Sauer U, Zamboni N, 2010. Ultrahigh performance liquid chromatography–tandem mass spectrometry method for fast and robust quantification of anionic and aromatic metabolites. Analytical chemistry 82 (11), 4403–4412. [PubMed: 20433152]

Chiaradonna F, Ricciardiello F, Palorini RJC, 2018. The nutrient-sensing hexosamine biosynthetic pathway as the hub of cancer metabolic rewiring. Cells 7 (6), 53. [PubMed: 29865240]

Das TM, Salangsang F, Landman AS, Sellers WR, Pryer NK, Levesque MP, Dummer R, McMahon M, Stuart DD, 2013. Modelling vemurafenib resistance in melanoma reveals a strategy to forestall drug resistance. Nature 494 (7436), 251–255. [PubMed: 23302800]

Deplus R, Delatte B, Schwinn MK, Defrance M, Mendez J, Murphy N, Dawson MA, Volkmar M, Putmans P, Calonne E, Shih AH, Levine RL, Bernard O, Mercher T, Solary E, Urh M, Daniels DL, Fuks F, 2013. TET2 and TET3 regulate GlcNAcylation and H3K4 methylation through OGT and SET1/COMPASS. EMBO J. 32 (5), 645–655. [PubMed: 23353889]

Emran AA, Marzese DM, Menon DR, Stark MS, Torrano J, Hammerlindl H, Zhang G, Brafford P, Salomon MP, Nelson N, Hammerlindl S, Gupta D, Mills GB, Lu Y, Sturm RA, Flaherty K, Hoon DSB, Gabrielli B, Herlyn M, Schaider H, 2018. Distinct histone modifications denote early stress-induced drug tolerance in cancer. Oncotarget 9 (9), 8206–8222. [PubMed: 29492189]

Fardini Y, Dehennaut V, Lefebvre T, Issad T, 2013. O-GlcNAcylation: a new cancer hallmark? Front. Endocrinol. 4, 99.

Feng J, Liu T, Qin B, Zhang Y, Liu XS, 2012. Identifying ChIP-seq enrichment using MACS. Nature protocols 7 (9), 1728–1740. [PubMed: 22936215]

Fong JJ, Nguyen BL, Bridger R, Medrano EE, Wells L, Pan S, Sifers RN, 2012. beta-N-Acetylglucosamine (O-GlcNAc) is a novel regulator of mitosis-specific phosphorylations on histone H3. J. Biol. Chem. 287 (15), 12195–12203. [PubMed: 22371497]

Fröhlich EE, Farzi A, Mayerhofer R, Reichmann F, Jačan A, Wagner B, Zinser E, Bordag N, Magnes C, Fröhlich E, Kashofer K, 2016. Cognitive impairment by antibiotic-induced gut dysbiosis: analysis of gut microbiota-brain communication. Brain, behavior, and immunity 56, 140–155. [PubMed: 26923630]

Gao J, Yang Y, Qiu R, Zhang K, Teng X, Liu R, Wang Y, 2018. Proteomic analysis of the OGT interactome: novel links to epithelial-mesenchymal transition and metastasis of cervical cancer. Carcinogenesis 39 (10), 1222–1234. [PubMed: 30052810]

Gelinas R, Dontaine J, Horman S, Beauloye C, Bultot L, Bertrand L, 2018. AMP-activated protein kinase and O-GlcNAcylation, two partners tightly connected to regulate key cellular processes. Front. Endocrinol. 9, 519.

Gelinas R, Mailleux F, Dontaine J, Bultot L, Demeulder B, Ginion A, Daskalopoulos EP, Esfahani H, Dubois-Deruy E, Lauzier B, Gauthier C, Olson AK, Bouchard B, Des Rosiers C, Viollet B, Sakamoto K, Balligand JL, Vanoverschelde JL, Beauloye C, Horman S, Bertrand L, 2018. AMPK activation counteracts cardiac hypertrophy by reducing O-GlcNAcylation. Nat. Commun. 9 (1), 374. [PubMed: 29371602]

Haass NK, Beaumont KA, Hill DS, Anfosso A, Mrass P, Munoz MA, Kinjyo I, Weninger W, 2014. Real-time cell cycle imaging during melanoma growth, invasion, and drug response. Pigment Cell Melanoma Res 27, 764–776. [PubMed: 24902993]

Hammerlindl H, Schaider H, 2018. Tumor cell-intrinsic phenotypic plasticity facilitates adaptive cellular reprogramming driving acquired drug resistance. J. Cell Commun. Signal. 12 (1), 133–141. [PubMed: 29192388]

Hata AN, Niederst MJ, Archibald HL, Gomez-Caraballo M, Siddiqui FM, Mulvey HE, Maruvka YE, Ji F, Bhang HE, Krishnamurthy Radhakrishna V, Siravegna G, Hu H, Raoof S, Lockerman E, Kalsy A, Lee D, Keating CL, Ruddy DA, Damon LJ, Crystal AS, Costa C, Piotrowska Z, Bardelli A, Iafrate AJ, Sadreyev RI, Stegmeier F, Getz G, Sequist LV, Faber AC, Engelman JA, 2016.

Tumor cells can follow distinct evolutionary paths to become resistant to epidermal growth factor receptor inhibition. Nat. Med. 22 (3), 262–269. [PubMed: 26828195]

Hinohara K, Wu HJ, Vigneau S, McDonald TO, Igarashi KJ, Yamamoto KN, Madsen T, Fassl A, Egri SB, Papanastasiou M, Ding L, Peluffo G, Cohen O, Kales SC, Lal-Nag M, Rai G, Maloney DJ, Jadhav A, Simeonov A, Wagle N, Brown M, Meissner A, Sicinski P, Jaffe JD, Jeselsohn R, Gimelbrant AA, Michor F, Polyak K, 2018. KDM5 histone demethylase activity links cellular transcriptomic heterogeneity to therapeutic resistance. Cancer Cell 34 (6), 939–953 e939. [PubMed: 30472020]

Hong A, Moriceau G, Sun L, Lomeli S, Piva M, Damoiseaux R, Holmen SL, Sharpless NE, Hugo W, Lo RS, 2018. Exploiting drug addiction mechanisms to select against MAPKi-resistant melanoma. Cancer Discov. 8 (1), 74–93. [PubMed: 28923912]

Hrit J, Goodrich L, Li C, Wang BA, Nie J, Cui X, Martin EA, Simental E, Fernandez J, Liu MY, Nery JR, Castanon R, Kohli RM, Tretyakova N, He C, Ecker JR, Goll M, Panning B, 2018. OGT binds a conserved C-terminal domain of TET1 to regulate TET1 activity and function in development. Elife 7.

Huson DH, Bryant D, 2006. Application of phylogenetic networks in evolutionary studies. Molecular biology and evolution 23 (2), 254–267. [PubMed: 16221896]

Itkonen HM, Urbanucci A, Martin SE, Khan A, Mathelier A, Thiede B, Walker S, Mills IG, 2019. High OGT activity is essential for MYC-driven proliferation of prostate cancer cells. Theranostics 9 (8), 2183–2197. [PubMed: 31149037]

Ito R, Katsura S, Shimada H, Tsuchiya H, Hada M, Okumura T, Sugawara A, Yokoyama A, 2014. TET3-OGT interaction increases the stability and the presence of OGT in chromatin. Genes Cells 19 (1), 52–65. [PubMed: 24304661]

Jia Y, Yun CH, Park E, Ercan D, Manuia M, Juarez J, Xu C, Rhee K, Chen T, Zhang H, Palakurthi S, Jang J, Lelais G, DiDonato M, Bursulaya B, Michellys PY, Epple R, Marsilje TH, McNeill M, Lu W, Harris J, Bender S, Wong KK, Janne PA, Eck MJ, 2016. "Overcoming EGFR(T790M) and EGFR (C797S) resistance with mutant-selective allosteric inhibitors. Nature 534 (7605), 129–132. [PubMed: 27251290]

Li H, Handsaker B, Wysoker A, Fennell T, Ruan J, Homer N, Marth G, Abecasis G, Durbin R, 2009. The sequence alignment/map format and SAMtools. bioinformatics 25 (16), 2078–2079. [PubMed: 19505943]

Liao Y, Smyth GK, Shi W, 2014. featureCounts: an efficient general purpose program for assigning sequence reads to genomic features. Bioinformatics 30 (7), 923–930. [PubMed: 24227677]

Lin YC, Lin CH, Yeh YC, Ho HL, Wu YC, Chen MY, Chou TY, 2018. High O-linked N-acetylglucosamine transferase expression predicts poor survival in patients with early stage lung adenocarcinoma. Oncotarget 9 (57), 31032–31044. [PubMed: 30123425]

Liu Y, Chen Q, Zhang N, Zhang K, Dou T, Cao Y, Liu Y, Li K, Hao X, Xie X, Li W, Ren Y, Zhang J, 2020. Proteomic profiling and genome-wide mapping of O-GlcNAc chromatin-associated proteins reveal an O-GlcNAc-regulated genotoxic stress response. Nat. Commun. 11 (1), 5898. [PubMed: 33214551]

Love MI, Huber W, Anders S, 2014. Moderated estimation of fold change and dispersion for RNA-seq data with DESeq2. Genome biology 15 (12), 1–21.

Manzano JL, Layos L, Buges C, de Los Llanos Gil M., Vila L., Martinez-Balibrea E., Martinez-Cardus A., 2016. Resistant mechanisms to BRAF inhibitors in melanoma. Ann. Transl. Med. 4 (12), 237. [PubMed: 27429963]

Martin SES, Tan ZW, Itkonen HM, Duveau DY, Paulo JA, Janetzko J, Boutz PL, Tork L, Moss FA, Thomas CJ, Gygi SP, Lazarus MB, Walker S, 2018. Structure-based evolution of low nanomolar O-GlcNAc transferase inhibitors. J. Am. Chem. Soc. 140 (42), 13542–13545. [PubMed: 30285435]

Micel LN, Tentler JJ, Tan AC, Selby HM, Brunkow KL, Robertson KM, Davis SL, Klauck PJ, Pitts TM, Gangolli E, Fabrey R, O'Connell SM, Vincent PW, Eckhardt SG, 2015. Antitumor activity of the MEK inhibitor TAK-733 against melanoma cell lines and patient-derived tumor explants. Mol. Cancer Ther. 14 (2), 317–325. [PubMed: 25376610]

Milanovic M, Fan DNY, Belenki D, Dabritz JHM, Zhao Z, Yu Y, Dorr JR, Dimitrova L, Lenze D, Monteiro Barbosa IA, Mendoza-Parra MA, Kanashova T, Metzner M, Pardon K, Reimann M, Trumpp A, Dorken B, Zuber J, Gronemeyer H, Hummel M, Dittmar G, Lee S, Schmitt CA, 2018. Senescence-associated reprogramming promotes cancer stemness. Nature 553 (7686), 96–100. [PubMed: 29258294]

Rachidi S, Wallace K, Li H, Lautenschlaeger T, Li Z, 2018. Postdiagnosis aspirin use and overall survival in patients with melanoma. J Am Acad Dermatol 78 (5), 949–956. [PubMed: 29317280]

Rambow F, Rogiers A, Marin-Bejar O, Aibar S, Femel J, Dewaele M, Karras P, Brown D, Chang YH, Debiec-Rychter M, Adriaens C, Radaelli E, Wolter P, Bechter O, Dummer R, Levesque M, Piris A, Frederick DT, Boland G, Flaherty KT, van den Oord J, Voet T, Aerts S, Lund AW, Marine JC, 2018. Toward minimal residual disease-directed therapy in melanoma. Cell 174 (4), 843–855 e819. [PubMed: 30017245]

Ramirez M, Rajaram S, Steininger RJ, Osipchuk D, Roth MA, Morinishi LS, Evans L, Ji W, Hsu CH, Thurley K, Wei S, Zhou A, Koduru PR, Posner BA, Wu LF, Altschuler SJ, 2016. Diverse drug-resistance mechanisms can emerge from drug-tolerant cancer persister cells. Nat. Commun. 7, 10690. [PubMed: 26891683]

Ravindran Menon D, Das S, Krepler C, Vultur A, Rinner B, Schauer S, Kashofer K, Wagner K, Zhang G, Bonyadi Rad E, Haass NK, Soyer HP, Gabrielli B, Somasundaram R, Hoefler G, Herlyn M, Schaider H, 2015. A stress-induced early innate response causes multidrug tolerance in melanoma. Oncogene 34 (34), 4448–4459. [PubMed: 25417704]

Roesch A, Fukunaga-Kalabis M, Schmidt EC, Zabierowski SE, Brafford PA, Vultur A, Basu D, Gimotty P, Vogt T, Herlyn M, 2010. A temporarily distinct subpopulation of slow-cycling melanoma cells is required for continuous tumor growth. Cell 141 (4), 583–594. [PubMed: 20478252]

Ramírez F, Ryan DP, Grüning B, Bhardwaj V, Kilpert F, Richter AS, Heyne S, Dündar F, Manke T, 2016. deepTools2: a next generation web server for deep-sequencing data analysis. Nucleic acids research 44 (W1), W160–W165. [PubMed: 27079975]

Sakaue-Sawano A, Kurokawa H, Morimura T, Hanyu A, Hama H, Osawa H, Kashiwagi S, Fukami K, Miyata T, Miyoshi H, Imamura T, Ogawa M, Masai H, Miyawaki A, 2008. Visualizing spatiotemporal dynamics of multicellular cell-cycle progression. Cell 132 (3), 487–498. [PubMed: 18267078]

Schreuer M, Jansen Y, Planken S, Chevolet I, Seremet T, Kruse V, Neyns B, 2017. Combination of dabrafenib plus trametinib for BRAF and MEK inhibitor pretreated patients with advanced BRAF(V600)-mutant melanoma: an open-label, single arm, dual-centre, phase 2 clinical trial. Lancet Oncol. 18 (4), 464–472. [PubMed: 28268064]

Shaffer SM, Dunagin MC, Torborg SR, Torre EA, Emert B, Krepler C, Beqiri M, Sproesser K, Brafford PA, Xiao M, Eggan E, Anastopoulos IN, Vargas-Garcia CA, Singh A, Nathanson KL, Herlyn M, Raj A, 2017. Rare cell variability and drug-induced reprogramming as a mode of cancer drug resistance. Nature 546 (7658), 431–435. [PubMed: 28607484]

Sharma SV, Lee DY, Li B, Quinlan MP, Takahashi F, Maheswaran S, McDermott U, Azizian N, Zou L, Fischbach MA, Wong KK, Brandstetter K, Wittner B, Ramaswamy S, Classon M, Settleman J, 2010. A chromatin-mediated reversible drug-tolerant state in cancer cell subpopulations. Cell 141 (1), 69–80. [PubMed: 20371346]

Sodi VL, Khaku S, Krutilina R, Schwab LP, Vocadlo DJ, Seagroves TN, Reginato MJ, 2015. mTOR/MYC axis regulates O-GlcNAc transferase expression and O-GlcNAcylation in breast cancer. Mol. Cancer Res. 13 (5), 923–933. [PubMed: 25636967]

Spoerri L, Beaumont KA, Anfosso A, Haass NK, 2017. Real-Time Cell Cycle Imaging in a 3D Cell Culture Model of Melanoma. Methods Mol Biol 1612, 401–416. [PubMed: 28634959]

Sun X, Bieber JM, Hammerlindl H, Chalkley RJ, Li KH, Burlingame AL, Jacobson MP, Wu LF, Altschuler SJ, 2022. Modulating environmental signals to reveal mechanisms and vulnerabilities of cancer persisters. Sci. Adv. 8 (4), eabi7711. [PubMed: 35089788]

Škalamera D, Dahmer M, Purdon AS, Wilson BM, Ranall MV, Blumenthal A, Gabrielli B, Gonda TJ, 2012. Generation of a genome scale lentiviral vector library for EF1α promoter-driven expression of human ORFs and identification of human genes affecting viral titer. PloS one 7 (12), e51733. [PubMed: 23251614]

Tahiliani M, Koh KP, Shen Y, Pastor WA, Bandukwala H, Brudno Y, Agarwal S, Iyer LM, Liu DR, Aravind L, Rao A, 2009. Conversion of 5-methylcytosine to 5-hydroxymethylcytosine in mammalian DNA by MLL partner TET1. Science 324 (5929), 930–935. [PubMed: 19372391]

Tietze JK, Forschner A, Loquai C, Mitzel-Rink H, Zimmer L, Meiss F, Rafei-Shamsabadi D, Utikal J, Bergmann M, Meier F, Kreuzberg N, Schlaak M, Weishaupt C, Pfohler C, Ziemer M, Fluck M, Rainer J, Heppt MV, Berking C, 2018. The efficacy of re-challenge with BRAF inhibitors after previous progression to BRAF inhibitors in melanoma: a retrospective multicenter study. Oncotarget 9 (76), 34336–34346. [PubMed: 30344946]

Trapannone R, Rafie K, van Aalten DM, 2016. O-GlcNAc transferase inhibitors: current tools and future challenges. Biochem Soc. Trans. 44 (1), 88–93. [PubMed: 26862193]

Tsoi J, Robert L, Paraiso K, Galvan C, Sheu KM, Lay J, Wong DJL, Atefi M, Shirazi R, Wang X, Braas D, Grasso CS, Palaskas N, Ribas A, Graeber TG, 2018. Multi-stage differentiation defines melanoma subtypes with differential vulnerability to drug-induced iron-dependent oxidative stress. Cancer Cell 33 (5), 890–904 e895. [PubMed: 29657129]

Uphoff CC, Drexler HG, 2002. Comparative PCR analysis for detection of mycoplasma infections in continuous cell lines. In Vitro. Cell Dev Biol Anim 38, 79–85. [PubMed: 11928999]

Uphoff CC, Drexler HG, 2004. Detecting Mycoplasma contamination in cell cultures by polymerase chain reaction. Methods Mol Med 88, 319–326. [PubMed: 14634244]

Valpione S, Carlino MS, Mangana J, Mooradian MJ, McArthur G, Schadendorf D, Hauschild A, Menzies AM, Arance A, Ascierto PA, Di Giacomo A, de Rosa F, Larkin J, Park JJ, Goldinger SM, Sullivan RJ, Xu W, Livingstone E, Weichenthal M, Rai R, Gaba L, Long GV, Lorigan P, 2018. Rechallenge with BRAF-directed treatment in metastatic melanoma: a multi-institutional retrospective study. Eur. J. Cancer 91, 116–124. [PubMed: 29360604]

Vella P, Scelfo A, Jammula S, Chiacchiera F, Williams K, Cuomo A, Roberto A, Christensen J, Bonaldi T, Helin K, Pasini D, 2013. Tet proteins connect the O-linked N-acetylglucosamine transferase Ogt to chromatin in embryonic stem cells. Mol. Cell 49 (4), 645–656. [PubMed: 23352454]

Vogel FC, Bordag N, Zügner E, Trajkovic-Arsic M, Chauvistré H, Shannan B, Váraljai R, Horn S, Magnes C, Siveke JT, Schadendorf D, 2019. Targeting the H3K4 demethylase KDM5B reprograms the metabolome and phenotype of melanoma cells. Journal of Investigative Dermatology 139 (12), 2506–2516. [PubMed: 31229500]

Wang J, Yao Z, Jonsson P, Allen AN, Qin ACR, Uddin S, Dunkel IJ, Petriccione M, Manova K, Haque S, Rosenblum MK, Pisapia DJ, Rosen N, Taylor BS, Pratilas CA, 2018. A secondary mutation in BRAF confers resistance to RAF inhibition in a BRAF(V600E)-mutant brain tumor. Cancer Discov. 8 (9), 1130–1141. [PubMed: 29880583]

Wu D, Cai Y, Jin J, 2017. Potential coordination role between O-GlcNAcylation and epigenetics. Protein Cell 8 (10), 713–723. [PubMed: 28488246]

Xu Q, Yang C, Du Y, Chen Y, Liu H, Deng M, Zhang H, Zhang L, Liu T, Liu Q, Wang L, Lou Z, Pei H, 2014. AMPK regulates histone H2B O-GlcNAcylation. Nucleic Acids Res. 42 (9), 5594–5604. [PubMed: 24692660]

Yuan P, Ito K, Perez-Lorenzo R, Del Guzzo C, Lee JH, Shen CH, Bosenberg MW, McMahon M, Cantley LC, Zheng B, 2013. Phenformin enhances the therapeutic benefit of BRAF(V600E) inhibition in melanoma. Proc. Natl. Acad. Sci. USA 110 (45), 18226–18231. [PubMed: 24145418]

Zou Y, Palte MJ, Deik AA, Li H, Eaton JK, Wang W, Tseng YY, Deasy R, Kost-Alimova M, Dancik V, Leshchiner ES, Viswanathan VS, Signoretti S, Choueiri TK, Boehm JS, Wagner BK, Doench JG, Clish CB, Clemons PA, Schreiber SL, 2019. A GPX4-dependent cancer cell state underlies the clear-cell morphology and confers sensitivity to ferroptosis. Nat. Commun. 10 (1), 1617. [PubMed: 30962421]

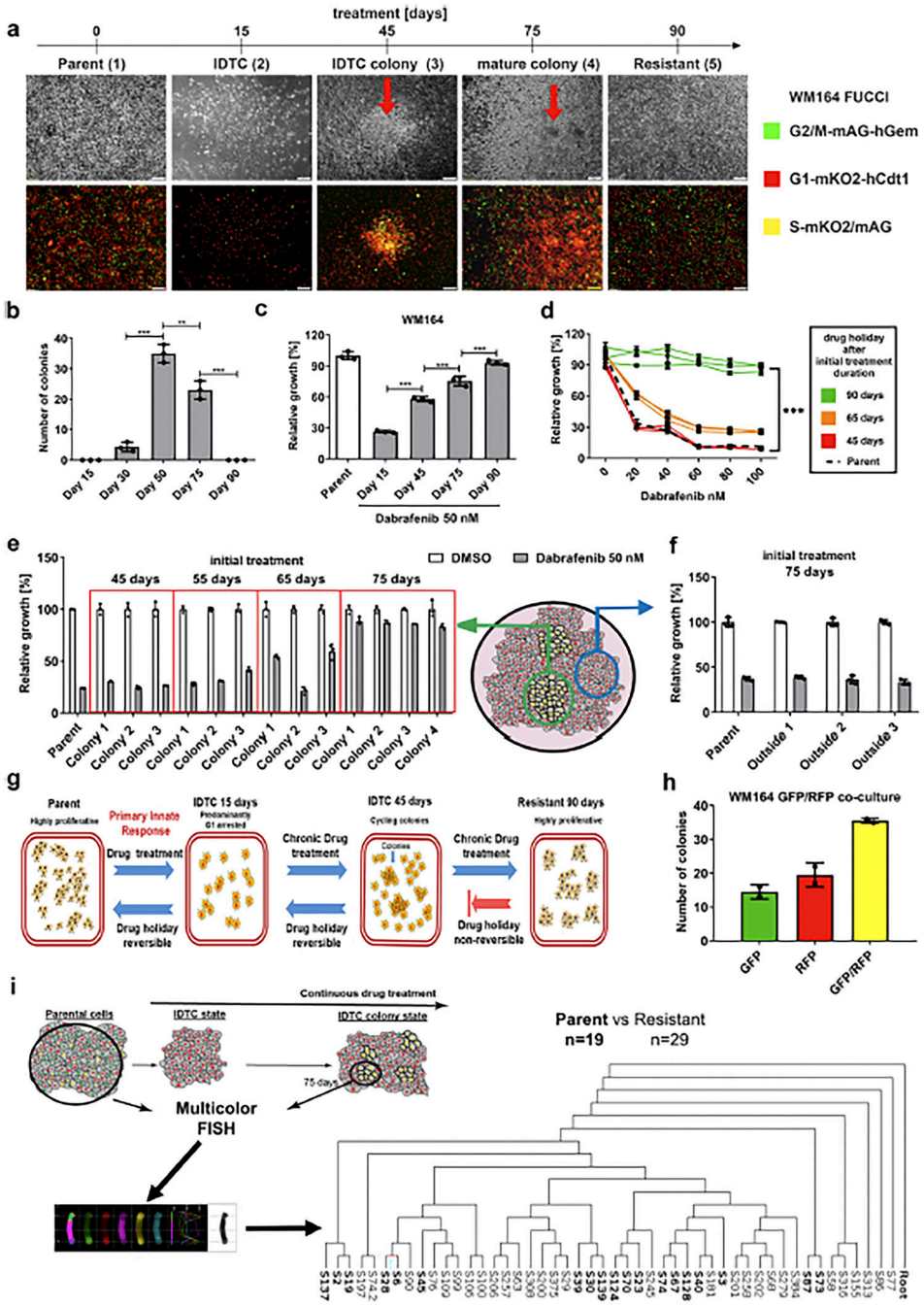

Fig. 1. Transient cell states precede the development of multi-clonal acquired drug resistance.

a, Representative bright field or combined fluorescence images (n ≥ 3 independent experiments) of FUCCI-WM164 cells exposed to dabrafenib 50 nM for the indicated time frames. mKO2-hCdt1 (red) indicates G1 phase, mAG-hGem (green) indicates G2/M and mKO2-mAG (yellow) indicates early S phase. Red arrows indicate re-proliferative cell clusters (IDTC colonies) that escape the drug-induced slow-cycling state. **b,** Number of IDTC colonies at indicated time points during chronic exposure of WM164 cells to dabrafenib 50 nM (n = 3), P-Values were calculated using one-way ANOVA, * ** P ≤

0.001, * * P ≤ 0.01, data are represented as mean ± SD. **c,** Relative growth rate at indicated time points during chronic exposure of WM164 cells to dabrafenib 50 nM measured by MTT assay (n = 3). P-Values were calculated using one-way ANOVA, * ** P ≤ 0.001, * * P ≤ 0.01, data are represented as mean ± SD. **d,** Re-treatment response of WM164 cells to indicated concentrations of dabrafenib (72 h treatment) subjected to 21 days of drug holiday after chronic exposure to dabrafenib 50 nM for the indicated time measured by MTT assay. P-Values were calculated using two-way ANOVA, * ** P ≤ 0.001. **e and f,** Re-treatment response of isolated IDTC colonies (**e**) or slow-cycling (**f**) WM164 cells to indicated concentrations of dabrafenib (72 h treatment) subjected to 21 days of drug holiday after chronic exposure to dabrafenib 50 nM for the indicated time measured by MTT assay (n = 3). Data are represented as mean ± SD. **g,** Model of reversibility of phenotypic transitions during chronic drug exposure. **h,** Number of IDTC colonies in a co-culture of GFP-positive and RFP-positive WM164 cells in a 1:1 ratio following 45 days of exposure to dabrafenib 50 nM that are either GFP-positive, RFP-positive, or double-positive (n = 2). Data are represented as mean ± SD. **i,** Phylogenetic tree of individual parental cells (n = 19, bold) and cells isolated from IDTC colonies after 75 days of exposure to dabrafenib 50 nM (n = 29), generated by analyzing chromosomal re-arrangements using whole chromosome FISH.

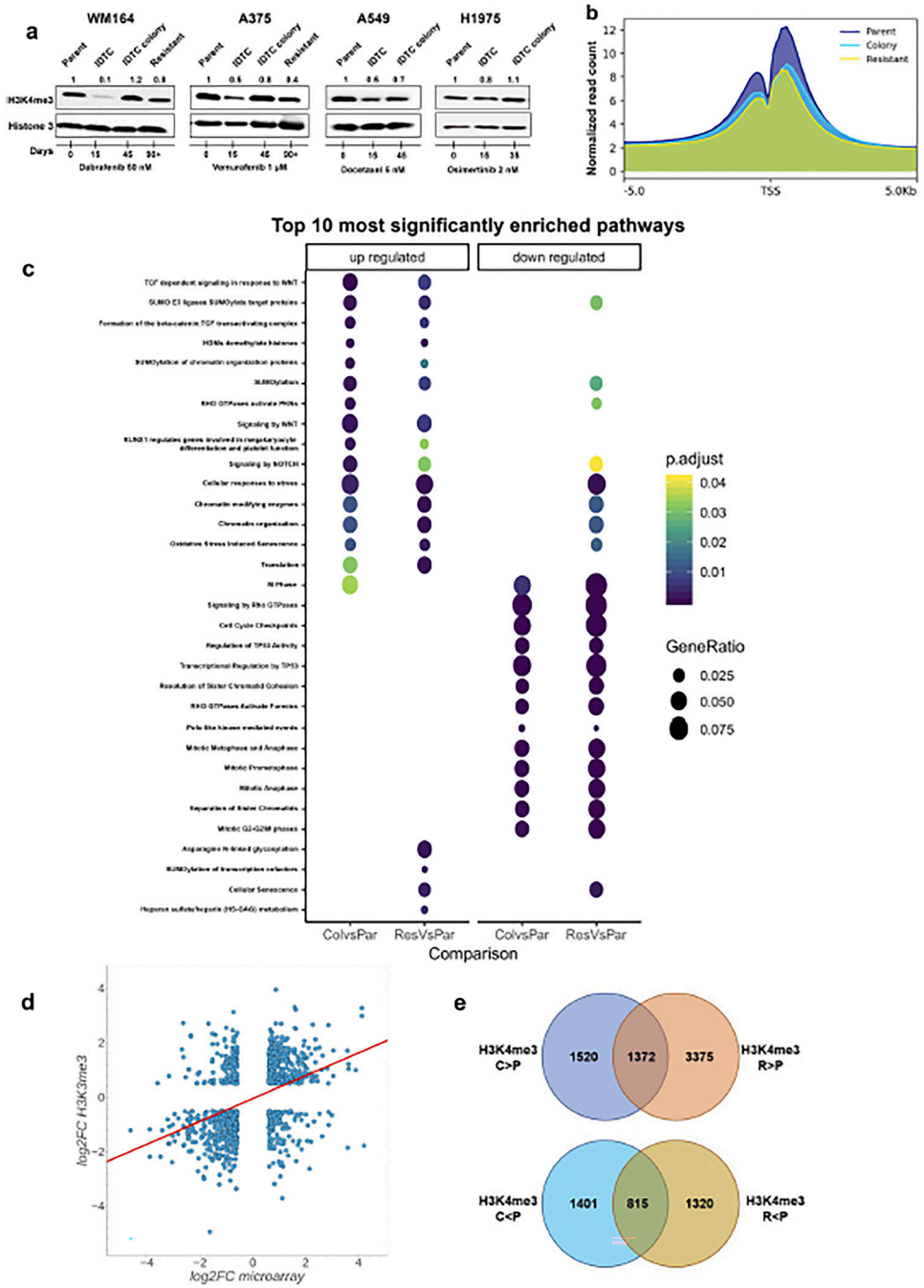

Fig. 2. H3K4me3 remodeling during the development of permanent acquired drug resistance.

a, Immunoblotting of H3K4me3 at the individual cell states in WM164, A375, A549 and H1975 cells. Histone 3 were used as loading control. Representative images of independent experiments are shown (n ≥ 2). **b,** Global H3K4me3 ChIP-seq profiles of parent, IDTC colony and resistant cells, replicates (all n = 2) were combined for visualization. ***c***, Over-representation analysis of genes annotated to significantly (FDR<5%) differentially marked proximal H3K4me3 peaks against Reactome pathways database of parent compared to IDTC colony or resistant. The top 10 most significantly enriched pathways are shown.

d, Scatter plot showing log2 fold change of differentially marked proximal H3K4me3 peaks (colony *vs* parental) as determined by ChIP-seq and mRNA expression levels of differentially expressed genes (colony *vs* parental) as determined by microarray. Shown are all genes that were significantly differentially expressed ($p \leq 0.05$, absolute log2FC ≥ 0.5) in both datasets. The slope is indicated by the red line. **e,** Venn diagrams comparing annotated genes with increased (**upper panel**) and decreased (**lower panel**) H3K4me3 in IDTC colony (Col) compared to parent (P) and resistant (R) compared to parent (P).

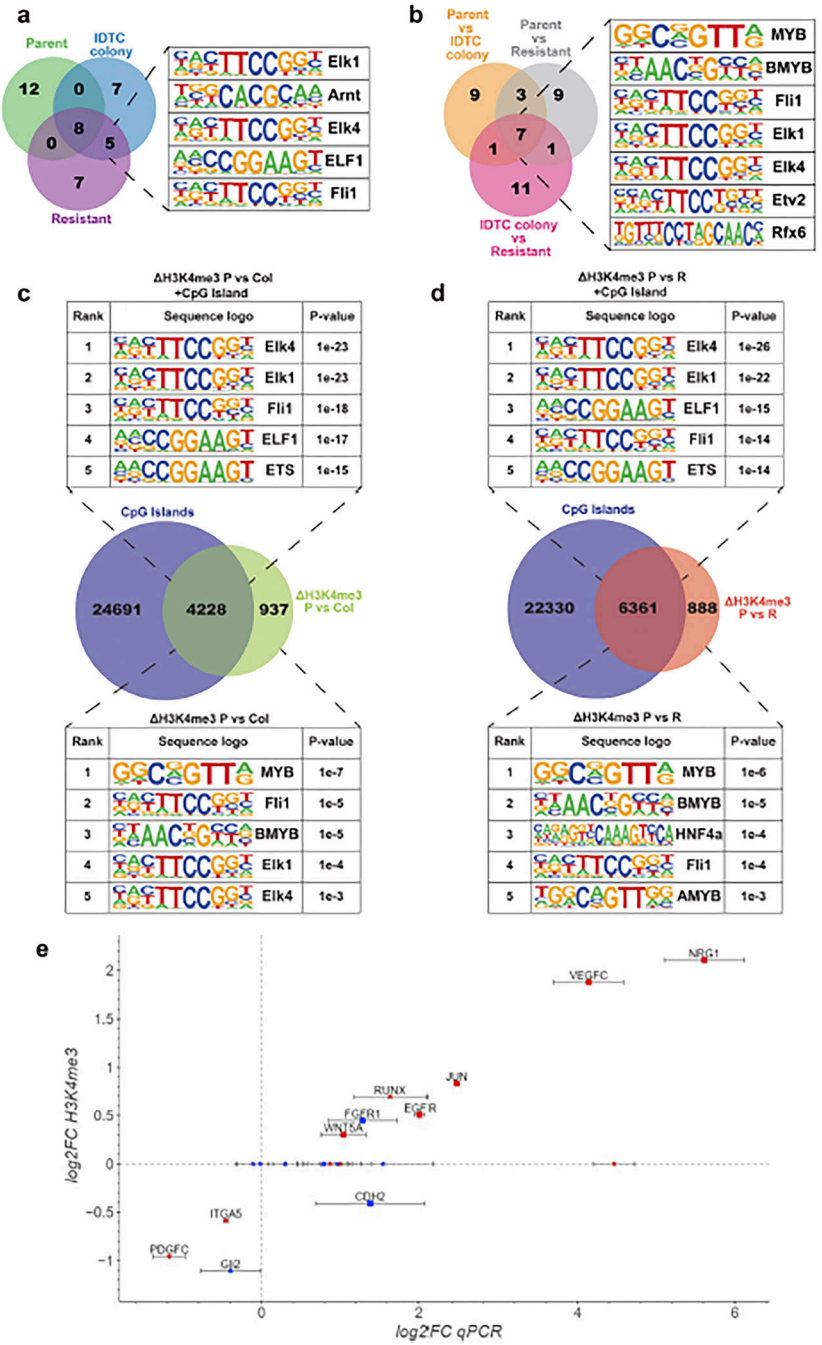

Fig. 3. Therapy induced H3K4me3 remodeling preferentially occurs at CpG island motifs.

a and b, Transcription factor binding motifs of proximal H3K4me3 peaks identified in IDTC colony and resistant cells (***a***) or significantly (FDR<5%) differentially marked proximal H3K4me3 peaks of all conditions (**b**). Top 20 most significantly discovered motifs were compared and commonly found sequence logos are shown. **c and d,** Venn diagram comparing annotated CpG islands from the USC genome browser for hg19 with significantly (FDR<5%) differentially marked proximal H3K4me3 peaks (ΔH3K4me3) of parent (P) *vs* IDTC colony (Col) (**c** middle panel) or parent (P) *vs* resistant (R) (**d** middle

panel). Top 5 transcription factor binding motifs identified in significantly differentially marked proximal H3K4me3 peaks (lower panel) and significantly differentially marked proximal H3K4me3 peaks that also overlap with CpG islands (upper panel) are shown. **e,** Scatter plot of log2FC of the differentially marked proximal H3K4me3 peaks of parent *vs* IDTC colony as determined by ChIP-seq and log2FC of mRNA levels as determined by RT-qPCR of 21 resistance-associated genes. Genes with significant changes in their mRNA level are indicated in red. Genes with H3K4me3 peaks overlapping with CpG islands are indicated by squares.

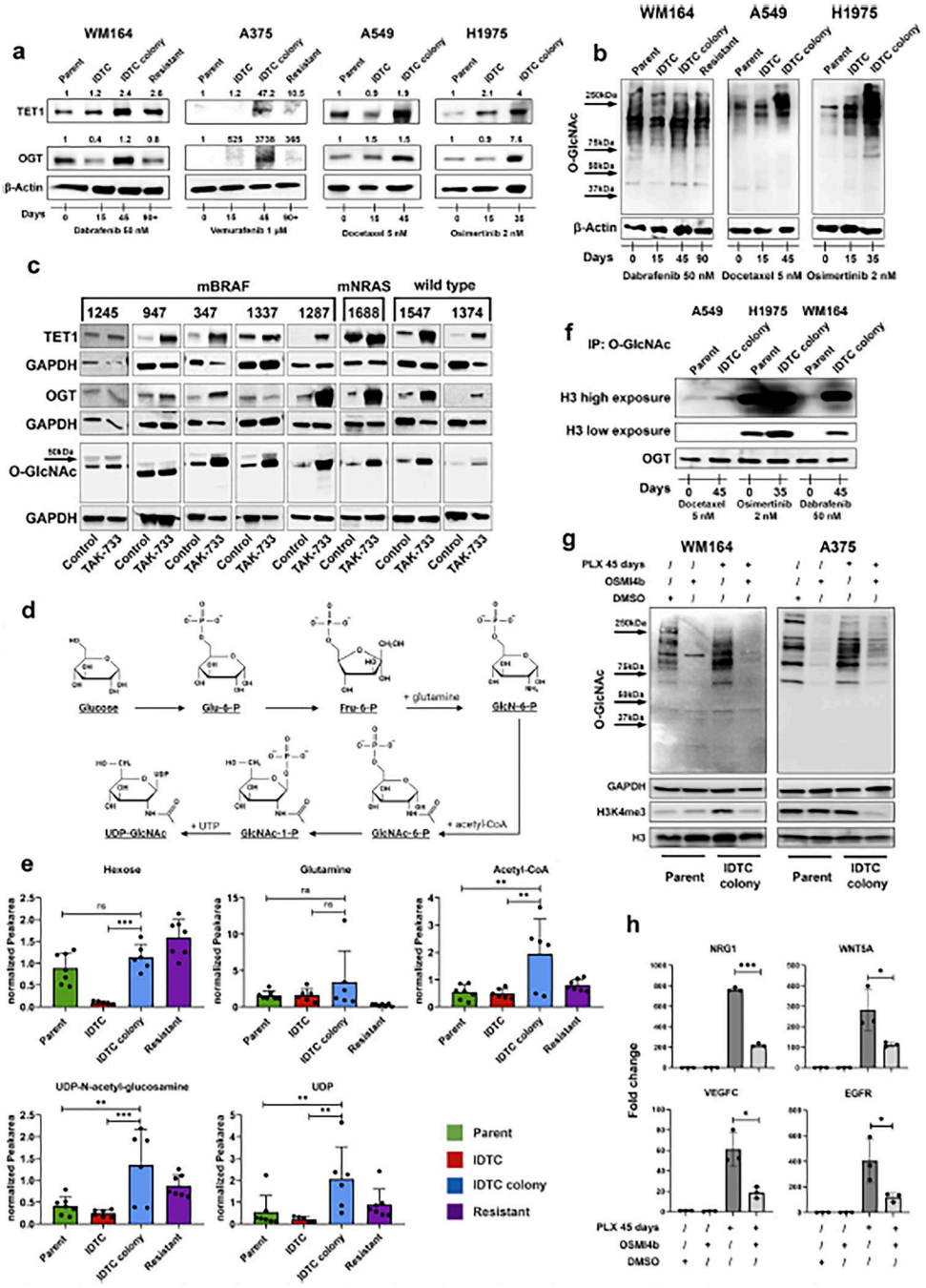

Fig. 4. Transiently resistant IDTC-colonies upregulate H3K4me3 through O-linked N-acetylglucosamine transferase.

Immunoblotting of OGT, TET1 (**a**) and O-GlcNAc (**b**) at the individual cell states in WM164, A375 (**a** only), A549 and H1975 cells. β-Actin was used as loading control. **c,** Immunoblotting of OGT, TET1 and O-GlcNAc in PDX tumors either untreated (control) or exposed to TAK-733 for 30 days. GAPDH was used as processing and loading control. Representative images are shown (n ≥ 2). **d**, Schematic representation of the hexosamine biosynthesis pathway. ***e***, Abundance of the indicated metabolites (QC normalized data) from

WM164 cells (IDTC and IDTC colony n = 6, parent and resistant n = 7) at individual cell states. P-Values were calculated using ANOVA, * ** $P \leq 0.001$, * * $P \leq 0.01$, * $P \leq 0.05$, n.s. $P > 0.05$, Data are represented as mean +SD. **f,** Immunoprecipitation of O-GlcNAcylated proteins in WM164, A549 and H1975 parent or IDTC colony cells followed by immunoblotting for histone 3. Cell lysates were normalized to total protein concentration, and OGT was used as an IP positive control. Representative images of independent experiments are shown ($n \geq 2$). **g**, Immunoblotting of O-GlcNAc and H3K4me3 after treatment with PLX4032 (1 μM) (45 days) or OSMI4B (10 μM) (48 h), alone or in combination (45 days). β-Actin and H3 was used as loading control. **h,** Transcript levels of NRG1, WNT5A, VEGFC and EGFR after treatment with PLX4032 (1 μM) (45 days) or OSMI4B (10 μM) (48 h), alone or in combination (45 days). P-Values were calculated using ANOVA, * ** $P \leq 0.001$, * * $P \leq 0.01$, * $P \leq 0.05$, n.s. $P > 0.05$, Data are represented as mean +SD.

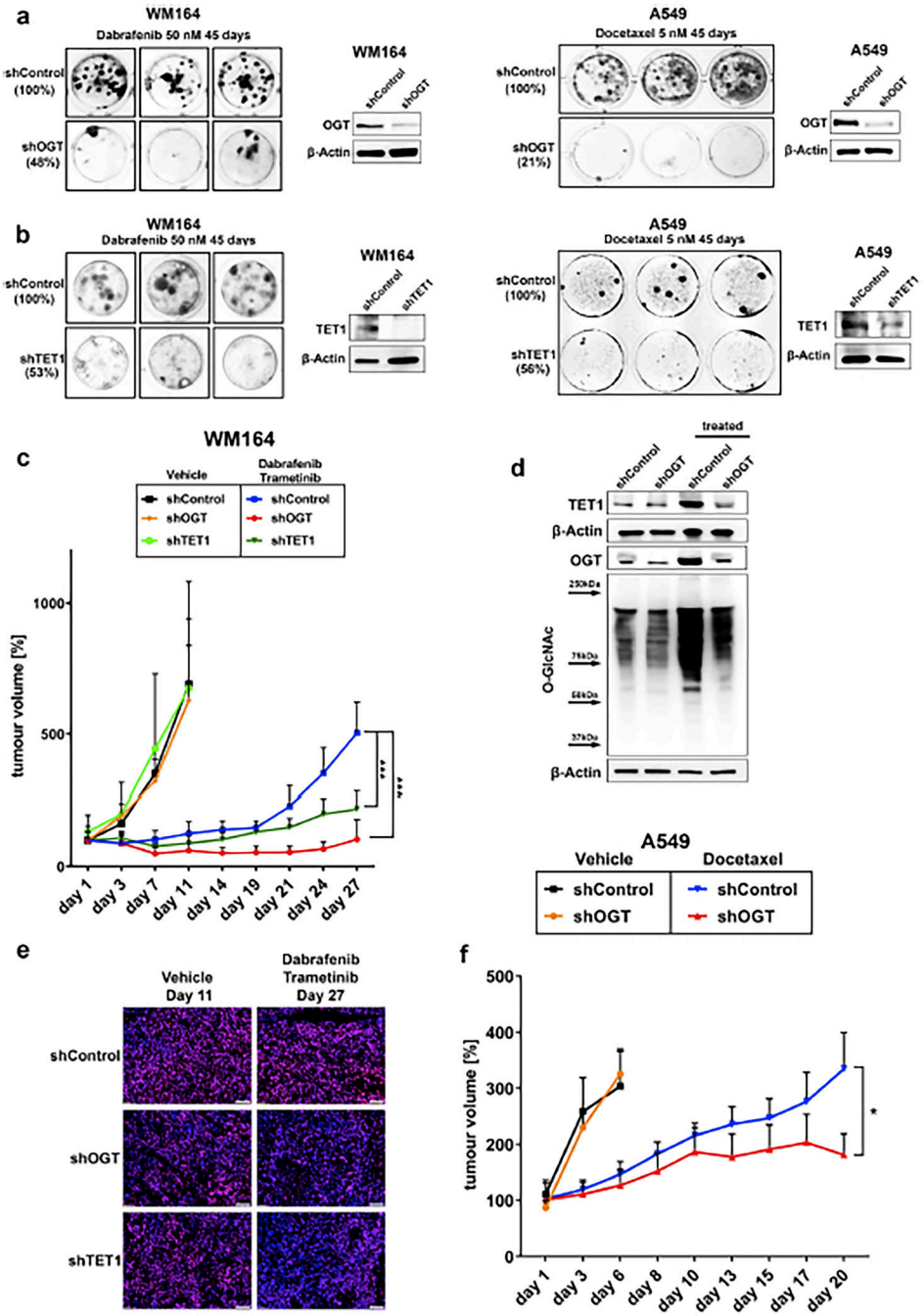

Fig. 5. Inhibition of OGT blocks therapy-induced cellular reprogramming preventing tumor recurrence.

a, Crystal violet staining of shOGT and shControl WM164 and A549 following exposure to dabrafenib (50nM) or docetaxel (5nM), respectively, for 45 days (left panels). Immunoblotting of OGT in WM164 and A549 (right panels) following transfection with shRNA targeting OGT. β-Actin was used as loading control. Representative images of independent experiments are shown (n≥2). **b**, Same as **(a)** with shTET1. Representative images of independent experiments are shown (n≥2). **c**, Tumor growth of WM164

shControl, shOGT and shTET1 cells injected into flanks of immunocompromised mice and treated with vehicle or dabrafenib (10 mg/kg)/trametinib (0.1 mg/kg), (n=6 per group). P-Values were calculated using t-tests corrected for multiple comparisons, *** $P \leq 0.001$, Data are represented as mean ±SD. **d**, Immunoblotting of OGT, TET1 and O-GlcNAc from isolated tumor samples treated with vehicle (11 days) or dabrafenib (10 mg/kg)/ trametinib (0.1 mg/kg) (treated, 27 days). β-Actin was used as loading control. Samples correspond to e and representative images of independent experiments are shown (n≥2). **e**, Immunofluorescence of H3K4me3 (red) combined with Hoechst nuclear staining (blue) of tumor samples treated with vehicle or dabrafenib (10 mg/kg)/trametinib (0.1 mg/kg). Representative images of independent experiments are shown (n≥3). **f**, Tumor growth of A549 shControl and shOGT cells injected into flanks of immunocompromised mice and treated with vehicle or docetaxel (15 mg/kg) (n=4 per group). P-Values were calculated using t-tests corrected for multiple comparisons, * $P \leq 0.05$. Data are represented as mean ±SD.

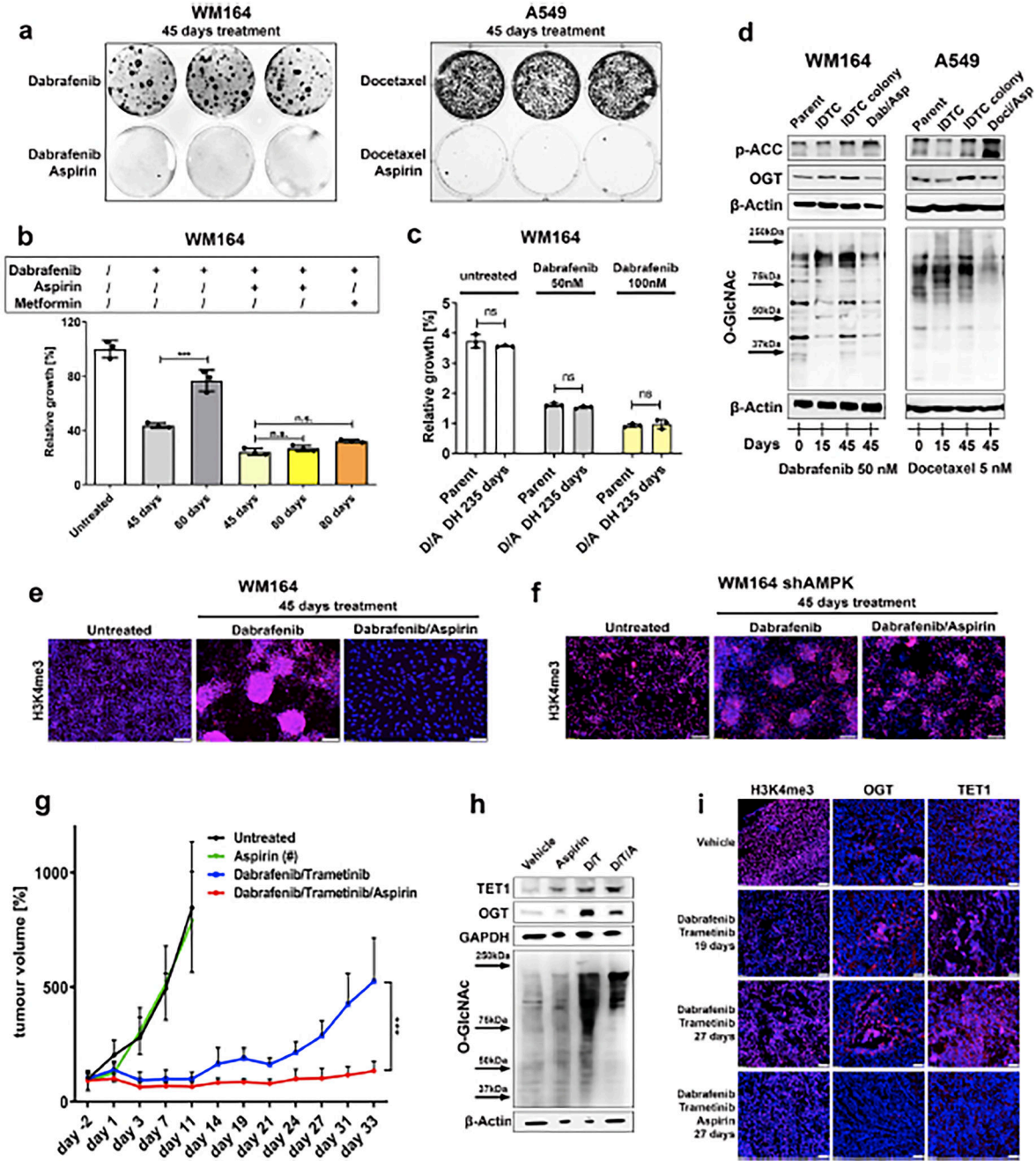

Fig. 6. AMP-activated protein kinase (AMPK) activation prevents OGT-mediated cellular reprogramming.

a, Crystal violet staining of WM164 and A549 cells exposed to dabrafenib 50 nM or docetaxel 5 nM with or without aspirin 2 mM for the indicated time frames. ***b,*** Relative growth rate of WM164 cells exposed to the indicated drug combinations for the indicated time points using MTT assay (n = 3). P-values were calculated using one-way ANOVA, * ** P ≤ 0.001, n.s. P > 0.05, Data are represented as mean ± SD. **c,** Relative growth rate of WM164 parental cells compared to WM164 cells exposed to dabrafenib 50 nM and aspirin 2 mM for 235 days, followed by 21 days drug holiday and re-treatment with

indicated dabrafenib concentrations for 72 h (n = 3). Data are represented as mean ± SD. **d,** Immunoblotting of phospho-acetyl-CoA carboxylase (p-ACC), OGT, TET1 and O-GlcNAc from WM164 and A549 cells following indicated treatments. β-Actin was used as loading control. Representative images of independent experiments are shown (n ≥ 2). **e and f,** Immunofluorescence staining of H3K4me3 (red) combined with Hoechst nuclear staining (blue) in WM164 shControl or shAMPK cells with indicated treatments. Representative images of independent experiments are shown (n ≥ 3). **g,** Tumor growth of WM164 cells that were treated *in vitro* with either dabrafenib 50 nM or dabrafenib 50 nM combined with aspirin 2 mM for 50 days before injection into immunocompromised mice (n = 3). P-values were calculated using t-tests corrected for multiple comparisons, * ** P ≤ 0.001, Data are represented as mean ± SD. **h,** Immunoblotting of OGT, TET1 and O-GlcNAc from isolated tumor samples treated with vehicle, aspirin (100 mg/kg), dabrafenib (10 mg/kg)/trametinib (0.1 mg/kg) or the combination. GAPDH was used as loading control. Representative images of independent experiments are shown (n ≥ 2). **i,** Immunofluorescence staining of H3K4me3, OGT and TET1 (all red) combined with Hoechst nuclear staining (blue) of tumor samples treated with vehicle, aspirin (100 mg/kg) dabrafenib (10 mg/kg)/trametinib (0.1 mg/kg) or the combination. Representative images of independent experiments are shown (n ≥ 3).